University of Mississippi

eGrove

2011

Design and Analysis of a Dielectric Resonator Antenna Array and Its Feed Network

John Ashmore

Follow this and additional works at: https://egrove.olemiss.edu/etd

Part of the Electrical and Computer Engineering Commons

DESIGN AND ANALYSIS OF A CYLINDRICAL DIELECTRIC RESONATOR ANTENNA

ARRAY AND ITS FEED NETWORK

A Thesis
presented in partial fulfillment of requirements
for the degree of Master of Engineering Science
in the department of Electrical Engineering
The University of Mississippi

by

JOHN ASHMORE

May 2011

ABSTRACT

There is an ever increasing need for smaller, lighter, more efficient antennas for commercial and military applications. One such antenna that meets these requirements is the Dielectric Resonator Antenna (DRA). In recent years there has been an abundance of research on the utilization of the DRA as a radiating element. However, its practical application – especially pertaining to DRA arrays – is still considered to be at its infancy. The purpose of this work is to present a systematic process to be used in the design, simulation, optimization, fabrication, and testing of a cylindrical DRA array including its associated feed network. The DRA array development cycle begins with a single cylindrical radiating element. Common DRA parameters such as DRA radius, feed type, feed location, and element spacing are investigated. A DRA element in this research is optimized for bandwidth and gain for use at x-band (8-12 GHz).

The antenna feed network, being an integral part of all antenna arrays, is also considered. The primary causes of impedance mismatch in the feed network are identified and techniques to improve performance are explored. An improvement in impedance bandwidth is gained through traditional transmission line matching methods. Ultimately, a 16 (4x4) element and 256 (16x16) element array is fabricated, tested, and compared to an existing commercial technology.

DEDICATION

This thesis is dedicated to my loving wife Brandi, who without her patience and support this thesis would not be possible. I would also like to thank my parents who encouraged me at an early age to work hard and follow my dreams.

TABLE OF CONTENTS

LIST OF FIGURES

INTRODUCTION

The antenna has become increasingly ubiquitous, largely stemming from its role in radar systems during World War II. The use of antennas has expanded far beyond military applications, being used in telecommunications, remote sensor systems, radio frequency identification (RFID), automobiles, and entertainment devices. The focus of this research is twofold; to investigate the performance of one type of antenna, the DRA, and to closely evaluate the properties of the feed network necessary to deliver power to the antenna array. A brief introduction to the antenna in general terms will initially be presented. This will cover basic theory of operation, types of antennas and their applications, and an introduction to array theory. The DRA will then be presented and discussed in detail. Relevant literature regarding the DRA will be reviewed and presented.

Discussion of the feed network will begin with an overview of transmission line theory. Common implementations of antenna feed networks will also be considered along with a discussion of their effect on antenna array performance.

The thought process and procedures used to design an optimized DRA array will be presented along with simulation results and comparison to near-field range data. Design and simulation of the feed network improvements will also be included. The final results will be discussed and compared to similar technologies to show the feasibility of the designs.

ANTENNA THEORY

The antenna in its simplest form is a device which transmits or receives electromagnetic energy. It can be thought of as a transducer that converts electric current to an electromagnetic wave, or vice versa. The foundations for all aspects of antenna theory come from theories presented by James Clerk Maxwell. Maxwell developed equations known as Maxwell's equations which describe in full the relationship between electric and magnetic forces, or electromagnetism. Maxwell also described how these electromagnetic waves may propagate through the air. This claim was later verified through experiment by German physicist Heinrich Hertz in 1887. Hertz discovered that electrical disturbances could be detected with a single loop of the proper dimensions for resonance that contains an air gap for sparks to occur. These electrical disturbances were generated from two metal plates in the same plane, each with a wire connected to an induction coil. This may be the earliest implementation of an antenna known as a "Hertzian dipole" [1]. By 1901, Guglielmo Marconi built an antenna for radio communication across the Atlantic. The transmitting antenna consisted of several vertical wires attached to the ground, while the receiving antenna was a 200 meter wire held up by a kite [2].

A good starting point in the discussion of antennas is how and why they radiate. A static electric charge has an electric field associated with it. Electric field lines extend

radially around the charge. These field lines have both a magnitude and direction component. If some outside force were to act upon this electric charge, it would accelerate and then continue at a constant velocity. This event will create a disturbance in the electric field associated with the charge. As the disturbance propagates outward from the charge a radiated field component is created. The diagram below shows how the field lines change as the disturbance propagates out to infinity.
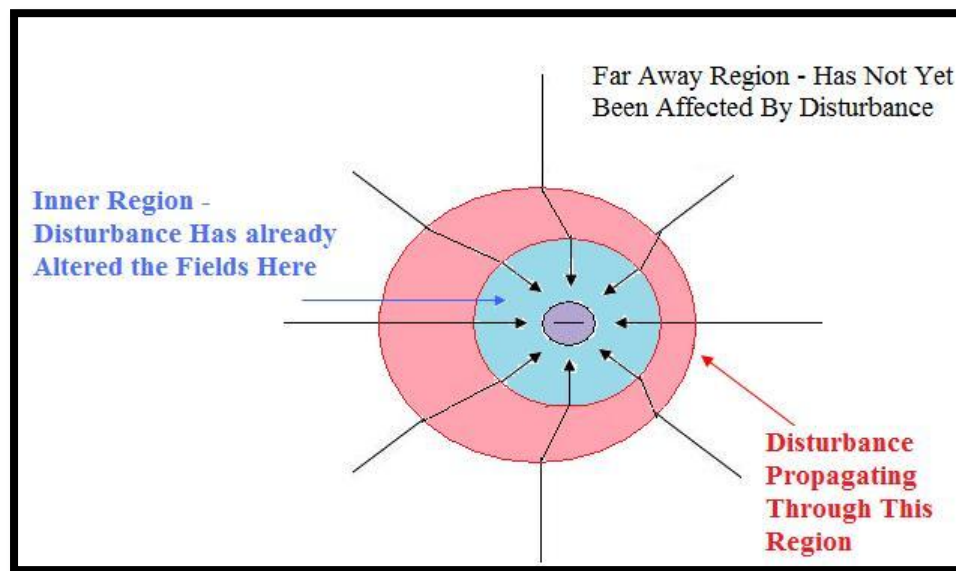
Figure 1. Electric Field Lines Disturbance [3]

In this diagram a negative charge has accelerated causing a disturbance. The blue region denotes the area in which the disturbance has already propagated leaving the altered field lines. The red region is the region in which the disturbance is currently propagating, altering the field lines as it moves outward. The white area represents the far away region which has yet to be affected by the disturbance. An easy to understand analogy of this phenomenon is that of a stone being dropped into a calm lake. The stone creates a disturbance, giving rise to a transient wave which propagates radially away from the impact point long after the stone has disappeared [1]. Electromagnetic waves,

3

however, travel at the speed of light, $c = 3.0 \times 10^8 \, m/s$. If a collection of charges is caused to oscillate (current flow), then radiation will be continuous. Antennas are designed to support these charge oscillations, thus explaining their effectiveness in radiating energy [1].

Presented below are the fundamental expressions used to evaluate the radiation fields of an antenna. The formulations are borrowed from [1]. It is assumed that the reader is familiar with Maxwell's equations and is referred to [2] or [1] for more detailed derivations of these expressions. Using Maxwell's equations as a starting point, the following vector potential function A can be derived.

$$A = \iiint_{v'} \mu J \frac{e^{-j\beta R}}{4\pi R} dv' \tag{1}$$

After finding A, the electric and magnetic field components can be calculated from

$$E = -j\omega A \tag{2}$$

$$E = \frac{1}{j\omega\epsilon} \nabla \times H \tag{3}$$

$$H = \frac{1}{\eta} \hat{r} \times E \tag{4}$$

$$H = \frac{1}{\mu} \nabla \times A \tag{5}$$

A general example used to show the process of calculating the near and far field and radiated power is that of the ideal dipole. An ideal dipole represents an infinitesimal element of current. The derivations presented here can be generalized for application to any antenna.

Consider an element of current with length Δz along the z-axis centered at the origin. It is of constant amplitude I. For this case, the volume integral of (1) becomes

$$A = \hat{z}\mu I \int_{-\frac{\Delta z}{2}}^{\frac{\Delta z}{2}} \frac{e^{-j\beta R}}{4\pi R} \, dz' \tag{6}$$

where μ is the permeability, β is the propagation constant, R is the distance from points on the current element to a field point P, and Δz is the length of the current element. The value of Δz is very small compared to both the wavelength and the distance R. Because of this, R is approximately equal to the distance r, which is the distance from the origin to the field point, for all points along Δz. Substituting r for R in (6) and integrating gives

$$A = \frac{\mu I e^{-j\beta r}}{4\pi r} \, \Delta z \, \hat{z} \tag{7}$$

The magnetic field can be found from (5) as

$$H = \frac{1}{\mu}\nabla \times (A_z\hat{z}) \tag{8}$$

Applying the vector identity $\nabla \times (f\boldsymbol{G}) = (\nabla f) \times \boldsymbol{G} + f(\nabla \times \boldsymbol{G})$ to (8) yields

$$H = \frac{1}{\mu}(\nabla A_z) \times \hat{z} + \frac{1}{\mu}A_z(\nabla \times \hat{z}) = \frac{1}{\mu}(\nabla A_z) \times \hat{z} \tag{9}$$

Substituting (7) into (9), we have

$$H = \nabla\left(\frac{I\Delta z e^{-j\beta r}}{4\pi r}\right) \times \hat{z} \tag{10}$$

Applying the gradient in spherical coordinates gives

$$H = \frac{I\Delta z}{4\pi}\frac{\partial}{\partial r}\left(\frac{e^{-j\beta r}}{r}\right)\hat{r} \times \hat{z} = \frac{I\Delta z}{4\pi}\left[-\frac{j\beta e^{-j\beta r}}{r} - \frac{e^{-j\beta r}}{r^2}\right]\hat{r} \times \hat{z}$$

$$= \frac{I\Delta z}{4\pi}\left[\frac{j\beta}{r} + 1/r^2\right]e^{-j\beta r}\sin\theta\hat{\phi} \tag{11}$$

The electric field can now be calculated from (3) as

$$E = \frac{I\Delta z}{4\pi}\left[\frac{j\omega\mu}{r} + \sqrt{\frac{\mu}{\epsilon}}\frac{1}{r^2} + \frac{1}{j\omega\epsilon r^3}\right]e^{-j\beta r}\sin\theta\hat{\phi} + \frac{I\Delta z}{2\pi}\left[\sqrt{\frac{\mu}{\epsilon}}\frac{1}{r^2} + \frac{1}{j\omega\epsilon}\frac{1}{r^3}\right]e^{-j\beta r}\cos\theta\hat{r} \tag{12}$$

5

If the medium surrounding the dipole is air or free space then β can be written as $\beta = \omega\sqrt{\mu_0\epsilon_0}$, where μ_0 and ϵ_0 are the permeability and permittivity of free space. Substituting this relationship into (11) and (12) and assuming that βr is large, then these equations can be reduced to

$$E = \frac{I\Delta z}{4\pi} j\omega\mu \frac{e^{-j\beta r}}{r} \sin\theta\, \widehat{\boldsymbol{\phi}} \tag{13}$$

$$H = \frac{I\Delta z}{4\pi} j\beta \frac{e^{-j\beta r}}{r} \sin\theta\, \widehat{\boldsymbol{\phi}} \tag{14}$$

These are the fields of an ideal dipole at large distances from the dipole and the ratio of the electric and magnetic field components is equal to the intrinsic impedance of the medium, $\eta = \sqrt{\frac{\mu}{\epsilon}}$.

Using the fields computed above, the expression for the complex power density flowing out of a sphere of radius r surrounding the dipole is

$$\begin{aligned}
S = \frac{1}{2}E \times H^* &= \frac{1}{2}\left(\frac{I\Delta z}{4\pi}\right)^2 j\omega\mu \frac{e^{-j\beta r}}{r}\sin\theta\, \widehat{\boldsymbol{\phi}} \\
&\times (-j\beta)\frac{e^{+j\beta r}}{r}\sin\theta\, \widehat{\boldsymbol{\phi}} = \frac{1}{2}\left(\frac{I\Delta z}{4\pi}\right)^2 \omega\mu\beta \frac{\sin^2\theta}{r^2}\, \hat{\boldsymbol{r}}
\end{aligned} \tag{15}$$

It should be noted that the expression of (15) is real valued and radially directed, which are both characteristics of radiations. If one wanted to compute the total power flowing out through a sphere of radius r surrounding the ideal dipole then it could be computed as

$$\begin{aligned}
P_f = \iint S \cdot ds &= \frac{1}{2}\left(\frac{I\Delta z}{4\pi}\right)^2 \omega\mu\beta \int_0^{2\pi} d\phi \int_0^{\pi} \sin^3\theta\, d\theta = \frac{1}{2}\left(\frac{I\Delta z}{4\pi}\right)^2 \omega\mu\beta 2\pi\frac{4}{3} \\
&= \frac{\omega\mu\beta}{12\pi}(I\,\Delta z)^2
\end{aligned} \tag{16}$$

This expression is the radiated power.

The equations derived in (11) and (12) are valid at any distance from the ideal dipole. For distances very close to the dipole such that $\beta r \ll 1$ or $r \ll \lambda$, only the dominant terms with the largest inverse powers of r need to be retained. The equations below are referred to as the near fields of the antenna.

$$\boldsymbol{H^{nf}} = \frac{I\Delta z e^{-j\beta r}}{4\pi r^2} \sin\theta \,\hat{\boldsymbol{\phi}} \tag{17}$$

$$\boldsymbol{E^{nf}} = -j\eta \frac{I\Delta z}{4\pi\beta} \frac{e^{-j\beta r}}{r^3} \sin\theta \,\hat{\boldsymbol{\phi}} - j\eta \frac{I\Delta z}{2\pi\beta} \frac{e^{-j\beta r}}{r^3} \cos\theta \,\hat{\boldsymbol{r}} \tag{18}$$

The complex power density using these fields can be computed using the complex Poynting vector expression.

$$\boldsymbol{S^{nf}} = \frac{1}{2}\left[E_\theta^{nf} H_\phi^{nf^*}\hat{\boldsymbol{r}} - E_r^{nf} H_\phi^{nf^*}\hat{\boldsymbol{\theta}}\right] = --\frac{j\eta}{2\beta}\left(\frac{I\Delta z}{4\pi}\right)^2 \frac{1}{r^5}\left(\sin^2\theta\,\hat{\boldsymbol{r}} + \cos\theta\sin\theta\,\hat{\boldsymbol{\theta}}\right) \tag{19}$$

This power density vector is imaginary and therefore has no time-average radial power flow. The imaginary power density corresponds to standing waves, rather than traveling waves associated with radiation, and indicate stored energy as in any reactive device [1].

The procedure detailed above can be extended to the case of a line source where the antenna length z' has a finite length and thus R cannot be assumed to equal r. Far-field conditions and radiation pattern parameters may be derived using the line source example.

ANTENNA TERMINOLOGY

There are several terms or parameters that are used to evaluate or describe antenna performance. The table below gives a list of the most important antenna parameters. Each parameter will be discussed in detail.

Table 1: Antenna Parameters

Directivity
Gain
Efficiency
Radiation Pattern
Polarization
Impedance
Bandwidth

Directivity: This can be thought of as a measure of the beam focusing ability of the antenna, commonly denoted as D. It is formally defined as the ratio of the maximum radiation intensity in the main beam to the average radiation intensity over all space [4]. An isotropic antenna is an example of an antenna with $D = 1$ since it radiates equally in all directions.

Gain: The gain of an antenna is the directivity reduced by any loss in the antenna. Contrary to how it may sound, gain is a passive phenomenon and does not add any additional power. It simply redistributes the power to provide more power in a certain direction than in other directions [5].

Efficiency: This is the ratio of power radiated by the antenna to the amount of power delivered at the input terminal of the antenna. The power not radiated by the antenna is usually lost in some form of resistive loss, commonly heat.

Radiation Pattern: Commonly denoted $F(\theta, \phi)$, this parameter represents the geometric pattern of the relative field strengths of the field emitted by the antenna [5]. It

includes main lobes, side lobes, and any rear lobes that may be present. Antenna performance is usually evaluated based on its radiation pattern at some θ, ϕ.

Polarization: Polarization of an antenna is the direction of the electric field with respect to the earth's surface and is determined by the physical structure and orientation of the antenna [5]. The three types of polarization are linear, circular, and elliptical.

Impedance: The ratio of voltage to current at the antenna input terminals. Ideally, the impedance of the antenna is matched to the characteristic impedance of the feeding mechanism to maximize power delivered to the antenna.

Bandwidth: This is the range of frequencies over which the performance of the antenna meets its designated performance characteristics. The bandwidth is typically centered over an operating frequency, usually the antenna's resonant frequency.

ANTENNA TYPES

There are a myriad of antenna types. The type of antenna chosen for a given application is a function of the desired radiating frequency and minimum acceptable performance. All antennas can be divided into just four basic types by their performance as a function of frequency [1]. These four types are 1) electrically small antennas 2) broadband antennas 3) aperture antennas, and 4) resonant antennas. An explanation of each type will given along with specific antennas types that fall into each category.

Electrically small antennas are antennas in which the physical size of the antenna is very small with respect to its operating wavelength. Wheeler formally defined an electrically small antenna as one whose maximum dimension is less than $\frac{\lambda}{2\pi}$ [6]. This relation is often expressed as $ka < 1$, where $k = \frac{2\pi}{\lambda}$ and $a = $ radius of a sphere enclosing

the maximum dimension of the antenna. Defining properties of an electrically small antenna are very low directivity, low input resistance, high input reactance, and low radiation efficiency. Low directivity can be an advantage if omnidirectional behavior is desirable, but the low input resistance and high input reactance properties tend to be a big disadvantage of these antennas. In two of the most common electrically small antennas, the short dipole and small loop (shown below), the input resistance is very low and the input reactance is very high.
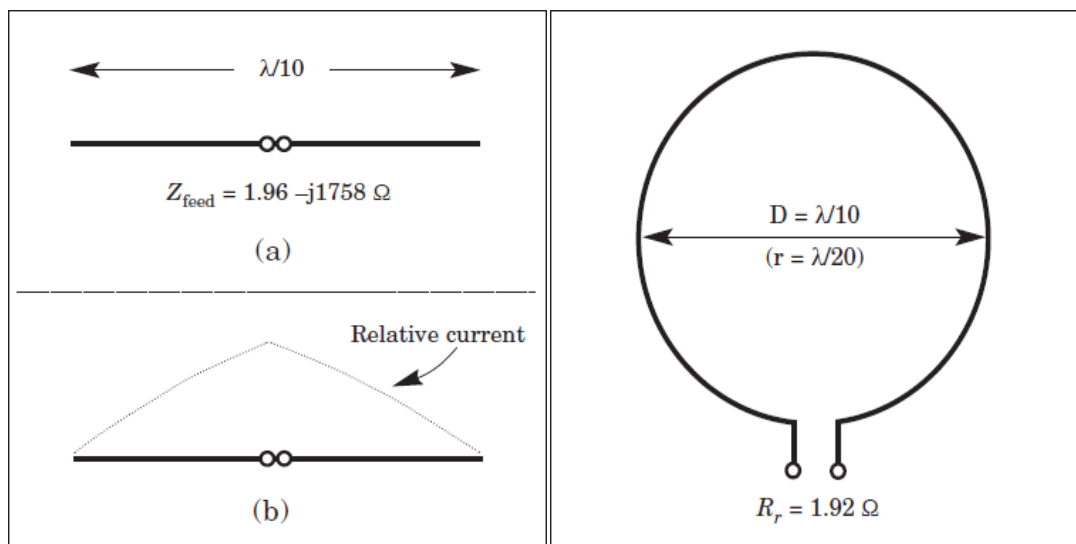
Figure 2. Short Dipole and Small Loop Antennas [7]

Matching the input impedance of these antennas is extremely difficult if not practically impossible. Due to the problems associated with electrically small antennas, it is desirable to avoid them when possible. A common example of an electrically small antenna is the whip antenna for AM reception on vehicles. At such low frequencies, antenna size comparable to a wavelength would not be practical. Even at higher frequencies, electrically small antennas may be necessary. RFID tags must be on the order of a few centimeters for many applications which would be considered electrically small for frequencies below 1 GHz.

The second type of antenna to be discussed is the broadband antenna. 'Broadband' is a term often used for a variety of antenna designs, but the term here indicates an antenna that has acceptable performance as measured with one or more parameters (pattern, gain, and/or impedance) over a 2:1 bandwidth ratio of upper to lower operating frequency [1]. Some properties of a broadband antenna are low to moderate gain, constant gain over a wide range of frequencies, real input impedance, and wide bandwidth. Broadband antennas are also known as travelling wave antennas, as opposed to resonant antennas which have standing waves. They are characterized by an active region that radiates the power. The travelling waves originate at the feed point and propagate outwards to the active region, where they are radiated. Examples of broadband antennas are spiral antennas, helical antennas, and log periodic dipole arrays.

Figure 3. Antennas of Various Types

The third type of antenna is the aperture antenna. An aperture antenna has an obvious physical aperture or opening through which electromagnetic waves flow.   These

antennas are typically characterized as having high gain, gain which increases with frequency, and moderate to wide bandwidth. Two of the most well known aperture antennas are the horn antenna and the reflector antenna. A horn antenna is composed of a rectangular waveguide feeding a walled aperture that is flared in one or two dimensions. If the walls are flared in both dimensions, it is called a pyramidal horn. The actual aperture formed by a horn is rectangular in geometry. A useful analogy of the horn antenna is that of a megaphone for acoustics. A megaphone provides directivity for sound waves just as the horn antenna provides directivity for electromagnetic waves. Horns are noteable for their high gain, low loss, and wide impedance bandwidth. Horns are commonly used in antenna test ranges as a standard measurement device for calibration purposes. Perhaps the most common use for horn antennas is for feeding reflector antennas. The dish antenna is an example of a reflector. It's diameter is typically several wavelengths and can be many wavelengths for high gain dish antennas. The dish antenna operates on geometric optics principals. Parameters such as diameter, focal length, and angle between focal point and edge of the dish drive the operation of this device. Transmitted waves from the focal point to any position on the parabolic dish will be reflected back in the same direction and in phase. This gives rise to the high directivity of parabolic dish reflectors. Another aperture type antenna is the slot antenna. These can be slots cut into a planar conductor such as microstrip, cavity backed slots where they are excited by a probe inserted into the cavity, or most notably slotted waveguides in which the waveguide itself acts as the feed structure to the slots cut from the waveguide walls. The size, shape, position, and orientation of the slots determine how they radiate.

The fourth and final type of antenna is the resonant antenna. Because this type of antenna includes the dielectric resonator antenna, a little more time will be spent in this section. The definition from [1] of a resonant antenna is a standing wave antenna with zero input reactance at resonance. The most common type of resonant antennas are wire antennas such as dipoles, vee dipoles, folded dipoles, Yagi-Udi arrays, and loop antennas. Figure 4 shows an arbitrary dipole antenna of length L and current I.
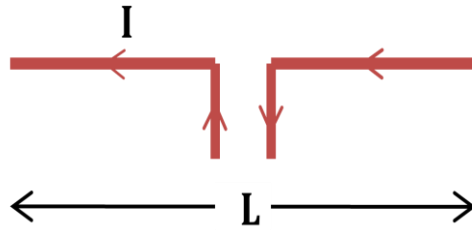
Figure 4. Dipole Antenna

The current distribution for this type antenna is assumed to be sinusoidal and it expressed as

$$I(z) = I_m sin\left[\beta\left(\frac{L}{2} - |z|\right)\right], \quad |z| < \frac{L}{2} \tag{20}$$

It can be shown that the input impedance for a half-wavelength infinitely thin dipole antenna $\left(L = \frac{\lambda}{2}\right)$, is $Z_a = 73 + j42.5 \ \Omega$ [1]. An inductive reactance exists in the input impedance for a dipole of exactly half-wavelength. By reducing the length of the dipole slightly however, the input impedance can be made purely real, leading to resonance. If L is reduced to 0.48λ then the dipole will resonate and the new input impedance will be $Z_a = 70 + j0 \ \Omega$. As mentioned above, this is for an infinitely thin dipole. As wire thickness is increased, the length must be further reduced to obtain resonance. Bandwidth can be improved by increasing wire thickness, however directivity is improved by increasing

13

length, so a compromise must be reached. The figures below show the real and imaginary impedance as a function of dipole length. Resonance occurs when the curves intersect the $Im[Z_a] = 0$ axis.
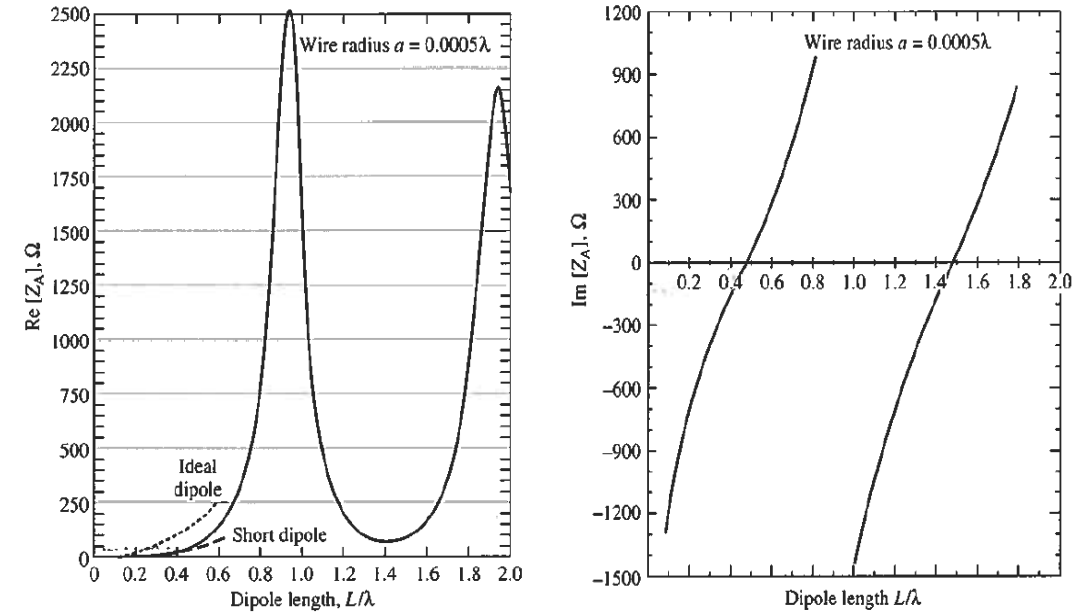
Figure 5. Real and Imaginary Impedance vs. Dipole Length [1]

Another popular resonant antenna structure is the microstrip patch antenna. Understanding the microstrip patch antenna is important as it shares many commonalities with the DRA. For instance, both are resonant structures, both are typically fed with microstrip line, and both are considered compact in size. Microstrip antennas were originally introduced in the early 1950s with work significantly picking up during the 1970s [8]. Since then, microstrip antennas have been extensively studied in academia and applied to numerous military and commercial applications. This is mainly due to their low profile, light weight, conformability and low cost. The basic microstrip patch element consists of a single patch of conductor on the upper surface of a grounded dielectric substrate. For resonance, some characteristic dimension of the patch is generally nearly

14

equal to one-half wavelength in the substrate medium [9]. Consider the patch below being fed by mictrostrip.
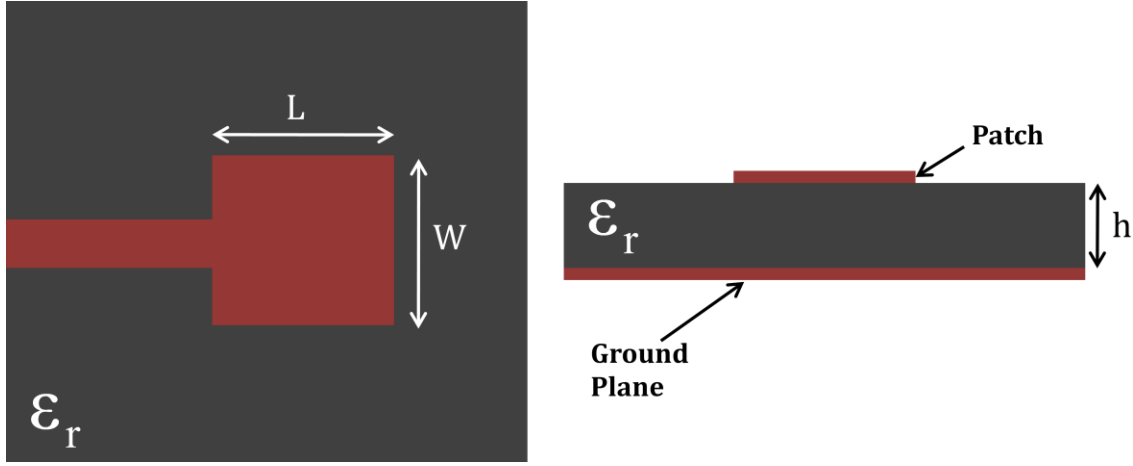
Figure 6. Microstrip Patch Antenna

The center frequency of the patch leads to the value of L being approximately equal to one-half wavelength within the dielectric medium (λ_d) [3].

$$f_c \approx \frac{c}{2L\sqrt{\epsilon_r}} \rightarrow L \approx \frac{1}{2}\frac{c}{f_c\sqrt{\epsilon_r}} = \frac{1}{2}\lambda_d \qquad (21)$$

Similar to the half-wave dipole, the length of a resonant half-wavelength patch is actually slightly less than $\frac{1}{2}\lambda_d$ due to fringing fields acting to extend the effective length of the patch [1]. The width W of the patch controls the impedance and also the radiation pattern of the antenna. By increasing W the impedance of the patch will be reduced. The fringing fields of a patch antenna are what cause it to radiate. The fringing fields can somewhat be controlled by the permittivity of the substrate, ϵ_r. Choosing a lower permittivity will yield increased radiation, improved bandwidth and efficiency. Raising the permittivity, however, will allow for reduction in size of the antenna which is often times desirable. Increasing the height h of the substrate can also improve bandwidth and efficiency, but has the drawback of producing surface waves in the substrate which is

undesirable [3]. The various feeding techniques for patch antennas could fill an entire book. Each feeding technique has its advantages and are often used to reduce some of the inherent drawbacks of patch antennas. Some of these techniques will be discussed later as they directly relate to feed methods for the DRA.

ARRAY THEORY

If one or more antenna elements are strategically placed next to one another, then their individual radiation patterns can be combined to synthesize properties only achievable with a much larger antenna, such as narrower beamwidth and increased gain. This collection of two or more elements is referred to as an antenna array. Antenna arrays are particularly useful in radar applications where a narrow highly directive beam is often required. Another major benefit of an array is the ability to change the phase for each individual radiating element. These arrays are called phased arrays. Phased arrays allow for electronic beam scanning which eliminates the need for mechanical steering of the antenna. Electronic beam scanning also allows for tracking of multiple targets in radar applications.

As already described, an individual antenna element has a specific radiation pattern. When two or more radiating elements are combined in an array configuration then the overall radiation pattern is changed. This is due to something called the array factor. The array factor describes the effect of combining multiple antenna elements in an array without taking into account each individual radiation pattern. The element pattern is combined with the array factor through a process called pattern multiplication to obtain the final radiation pattern for the array.

To illustrate how the array factor is calculated, consider the equal spaced linear array of isotropic radiators shown in Figure 7. The radiation fields of an isotropic radiator are proportional to $I_0 \frac{e^{-j\beta r}}{4\pi r}$ [1]. The path length difference or phase term for each element is represented by the term $e^{j\beta n d cos\theta}$, where d is the distance between elements, β is the propagation constant, n is the element number starting with $n = 0$, and θ is the angle between the z axis and the incoming wave front. The array factor AF for this linear array of isotropic elements can be found as

$$AF = I_0 + I_1 e^{j\beta d cos\theta} + I_2 e^{j\beta 2 d cos\theta} + \cdots = \sum_{n=0}^{N-1} I_n e^{j\beta n d cos\theta} \qquad (22)$$
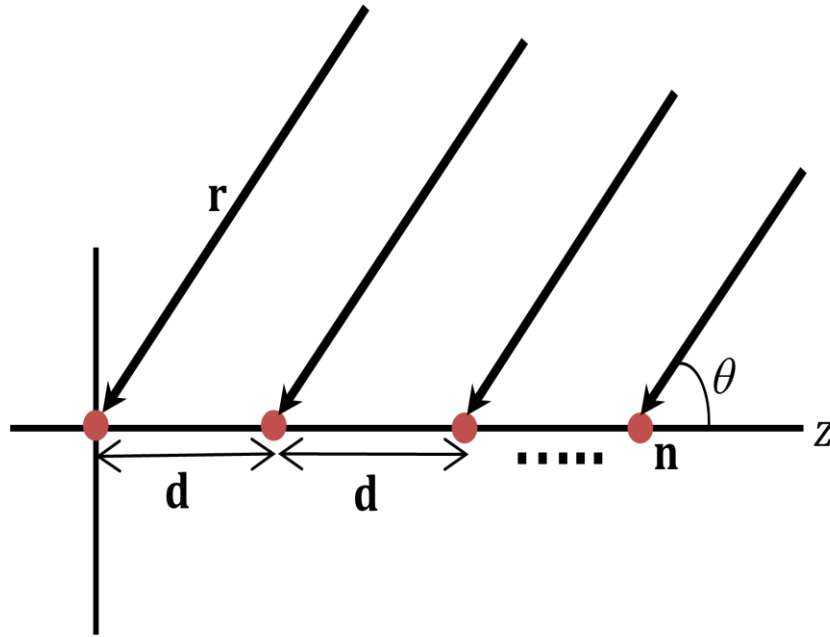
Figure 7: Equally spaced linear array of isotropic elements

Now consider the array to be transmitting. If the current has a linear phase progression, the phase can be separated explicitly as [1]

$$I_n = A_n e^{jn\alpha} \tag{23}$$

where the $n + 1^{th}$ element leads the nth element in phase by α. Equation (22) then becomes

$$AF = \sum_{n=0}^{N-1} A_n e^{jn(\beta d \cos\theta + \alpha)} \tag{24}$$

From this equation it is seen that the array factor is dependent on the number of radiating elements, the spacing between these elements, and the amplitude and phase of the applied signal to each element. The plots borrowed from [10] below show how these different array properties affect the radiation pattern. The plots are of directivity in dB vs. angle θ.
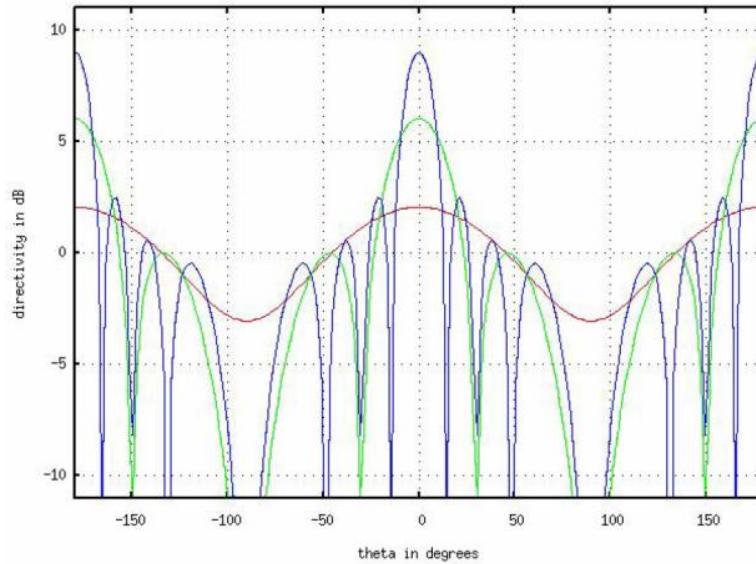
Figure 8: 2 (red), 5 (green), 10 (blue) element array with 0.4λ element spacing
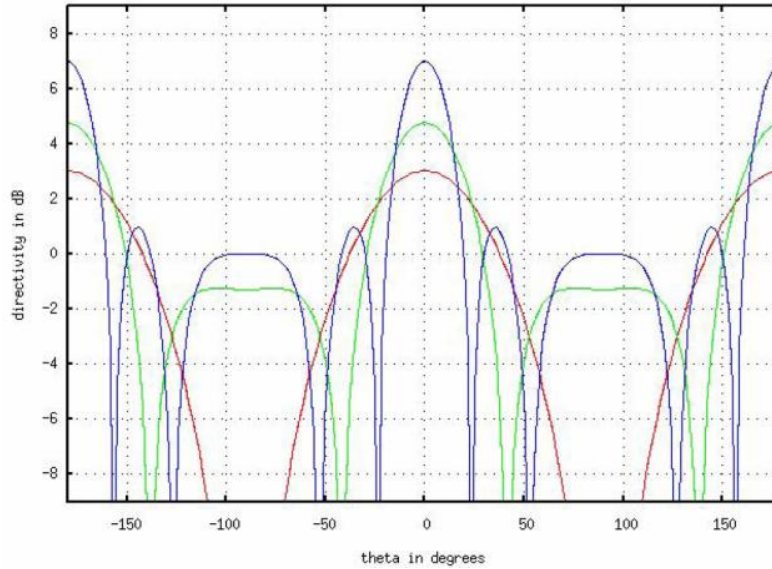
Figure 9: 5 Element Array With 0.2 (red), 0.3 (green), 0.5 (blue) time λ element spacing

These figures show that directivity and number of sidelobes is increased with increasing element numbers. As element spacing is increased, directivity and sidelobes are also increased.   An element spacing of 0.5λ gives good directivity with relatively low sidelobes. As element spacing is increased even further, the directivity will continue to increase, but a point will eventually be reached where grating lobes occur. Grating lobes are unwanted peaks in the beam pattern equal in amplitude to the main beam.

Another antenna characteristic particularly important in design of antenna arrays is broadside vs. endfire radiation. Broadside radiation is when the main beam of the antenna is normal to the plane containing the array elements. Endfire radiation occurs when the main beam is directed in the same plane as that of the array elements. Generally, the array factor for a broadside array produces a fan beam. For applications that require a single pencil beam an endfire array can be designed. The value of θ for which the array factor is

19

maximum will be represented by θ_0. For endfire condition, $\theta_0 = 0°\ or\ 180°$, which corresponds to $\alpha = -\beta d\ or + \beta d$. An array satisfying these conditions is known as an ordinary endfire array. If the spacing d is a half-wavelength, there will be two identical endfire lobes [1]. However, this extra lobe can be eliminated by reducing the element spacing to below a half-wavelength. The condition on spacings for an ordinary enfire array can be determined from

$$d \le \left(1 - \frac{1}{2N}\right)$$

(25)

The arrays considered up to this point have been linear arrays. Linear arrays have certain limitations, which can be overcome with multidimensional arrays. One limitation is that linear arrays can only be phase scanned in the plane along the line of element centers. The beamwidth in a line orthogonal to the center line is determined by the element pattern and cannot be adjusted. This limits the gain achievable with a linear array. A two-dimensional array however can be phase scanned in two planes and the beamwidth can also be adjusted in both planes allowing for a very narrow pencil beam and high gain. Multidimensional arrays can be arranged on surfaces of various geometries such as rectangular or circular. The grid pattern can also be varied, with equal or unequal element spacing in both or either directions. Like the linear array, if elements are similar, the array factor can be derived and used in pattern multiplication to calculate the total array pattern. Consider an arbitrary three-dimensional array with the position vectors from the origin to the *mn*th element.

$$\boldsymbol{r'_{mn}} = x'_{mn}\,\widehat{\boldsymbol{x}} + y'_{mn}\widehat{\boldsymbol{y}} + z'_{mn}\widehat{\boldsymbol{z}}$$

(26)

The array factor for a general multidimensional array on a surface is then [1]

$$AF(\theta, \phi) = \sum_{n=1}^{N} \sum_{m=1}^{M} I_{mn} e^{j(\beta \hat{r} \cdot r'_{mn} - \alpha_{mn})} \qquad (27)$$

The assumption made thus far has been that each element in an array is electrically isolated from each other element. In reality this is not the case. The interaction that exists between elements is referred to as mutual coupling. Mutual coupling affects the current magnitude, phase, and distribution along with element impedances. Mutual coupling also changes with frequency and scan angle. Mutual coupling presents itself in one of three ways: direct coupling through space between adjacent elements, indirect coupling by scattering from nearby objects, and path coupling from the feed network feeding each element [1]. Mutual and self impedances of an N port network can be found using conventional circuit analysis. The mutual impedance Z_{mn} can be found by dividing the open circuit voltage at terminal m by the current supplied to terminal n when all other terminals are open circuited. In practice, for a multi-element array mutual impedance is very difficult to measure or compute. For this reason numerical methods are typically used to solve for the effects of mutual coupling. Mutual coupling can be reduced by increasing the element spacing as approximately $\frac{1}{d^2}$. This is not always an option however, because increasing element spacing increases the size of the antenna. Mutual coupling is usually unavoidable in antenna arrays and must therefore be taken into account when designing an array.

The last array topic to be covered is that of phased arrays. As already mentioned, phased arrays allow for electronic beam steering by varying the phase or time delay to each element. For the purposes of this work, consider the diagram of a generic phased array antenna below.
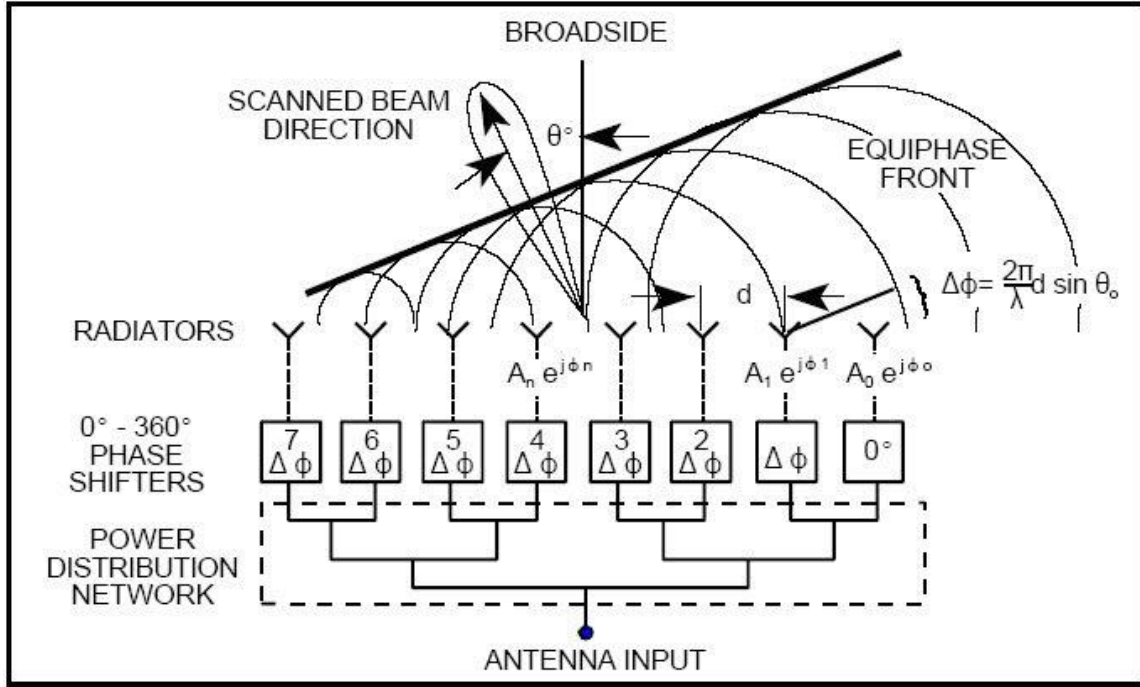
Figure 10: Phased Array Antenna [11]

This diagram shows an eight element array being corporately fed. Each element has its own phase shifter and attenuator for control of phase and amplitude. In the diagram, the beam is being steered $\theta°$ left of broadside. This is done by varying the phase difference $\Delta\phi$ between each consecutive element. The phase front of the 1st element leads that of the 8th element by $7\Delta\theta$, resulting in a beam steered in the direction shown. Using this technique, adjustments can be made to the phase shifters and attenuators to scan a sizeable portion of the forward looking area with varying beam shapes.

THE DIELECTRIC RESONATOR ANTENNA

Before the DRA was discovered, the dielectric resonator (DR) was being used as a high Q-factor (low loss) element for circuit applications such as oscillators and filters [12]. The DR is typically designed as a ceramic cylindrical puck with dielectric constant $\epsilon_r > 20$ in order to preserve a low loss compact design [13]. For oscillator and filter applications the DR was commonly metallically shielded to prevent radiation and maintain its high Q-factor. The DR was not thoroughly investigated for its radiating properties until 1983 when Long, et. al. [14] published a paper detailing the radiation characteristics of a cylindrical dielectric cavity antenna. The motivation for investigating the DR as a radiating element stemmed from the rapid increase in operating frequencies required for new applications. At frequencies beyond microwave in the millimeter wave band, conduction losses in metallic antennas become too great for efficient operation. Long et. al. proposed that by lowering the dielectric constant to values of $5 \leq \epsilon_r \leq 20$ and choosing appropriate cylinder dimensions and feed location, the radiation fields of a DR could be enhanced to produce an efficient DRA. Long et. al. derived a simple theoretical solution for the fields inside a cylindrical DRA using magnetic wall boundary conditions. The theoretical calculations were compared to measured results and correlated quite well.

The major characteristics and advantages of DRAs are presented in the bulleted list below.

- DRA size is proportional to $\frac{\lambda_0}{\sqrt{\epsilon_r}}$, where λ_0 is the free space wavelength at the resonant frequency, and ϵ_r is the dielectric constant of the material [15].

- The resonant frequency and radiation Q-factor is affected by the aspect ratio of the DRA for a fixed dielectric constant, allowing added design flexibility [15].

- Due to an absence of surface waves and minimal conductor losses, the DRA can maintain high radiation efficiency at extremely high frequencies [15].

- A wide range of dielectric constants can be used, allowing the designer to have control over the physical size and bandwidth of the DRA [15].

- Several feeding mechanisms can be used to excite the DRA, making them amenable to integration with various existing technologies [13].

- The DRA can have a much wider impedance bandwidth than microstrip antennas.

- Various modes can be excited, producing broadside or conical-shaped radiation patterns for different coverage requirements [15].

DRA THEORY AND ANALYSIS

DRAs can be fabricated in any number of shapes and sizes. The primary shapes used in practice are hemispherical, cylindrical, and rectangular. Each of these shapes must be modeled differently and only the hemispherical DRA has a closed form solution for determining input impedance. When designing a DRA the properties of primary interest are resonant frequency, input impedance, and radiation pattern. Because only the hemispherical DRA has an exact solution, approximate solutions must be developed for other geometries. Focusing on the cylindrical DRA, a brief look at the important parameters of design will be detailed. A brief discussion of analytical methods developed

for cylindrical DRA design will follow. The figure below shows a generic cylindrical DRA with a probe feed. The parameters of interest are labeled.
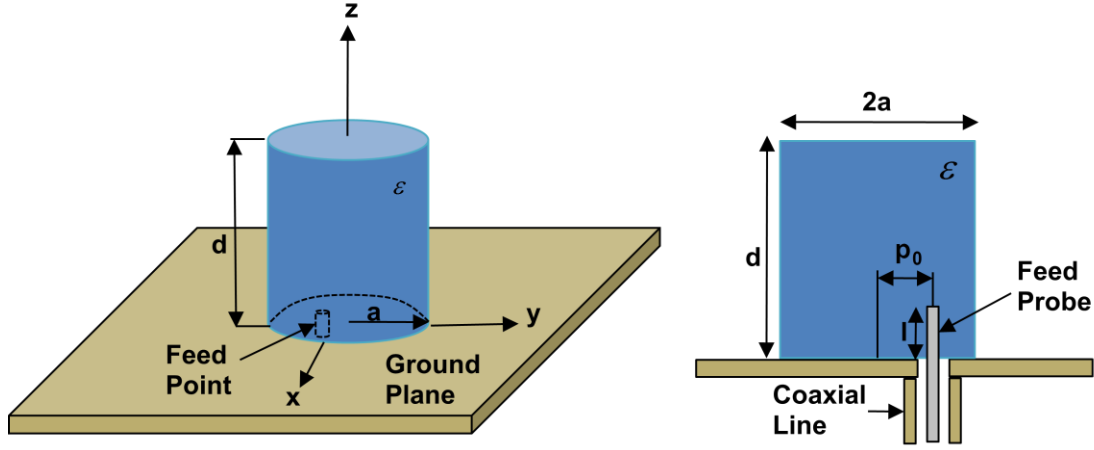
Figure 11: Cylindrical DRA Geometry

The resonant frequency and radiating Q-factor of a DRA depends on all of the parameters shown in Figure 11 and also the mode of propagation. A mode is defined as the electromagnetic field pattern exhibited inside of the DRA due to shape and boundary conditions of the element. The mode of propagation is important as it affects how well the DRA will radiate as well as the radiation pattern.   There are four natural modes of a cylindrical dielectric cavity, which are classified as $TE_{mn\delta}$, $TM_{mn\delta}$, $HE_{mn\delta}$, $EH_{mn\delta}$. TE and TM stand for transverse electric and transverse magnetic, meaning that the electric and magnetic fields, respectively, are transverse to the direction of propagation. HE and EH modes are called hybrid modes because they have non-vanishing electric and magnetic field components in the direction of propagation.   The first subscript, m denotes the number of full-period field variations in the azimuthal direction, while n denotes the number of radial variations. The subscript δ represents the number of half-wavelength variations in the axial direction and ranges between zero and one, approaching one for high

values of dielectric constant [15]. Different modes can be excited by using different feed techniques, but the most commonly used radiating modes are the $TM_{01\delta}$, $TE_{01\delta}$, and $HE_{11\delta}$ modes.

As already mentioned the cylindrical DRA cannot be solved for using any known closed form solution, so approximation models are used. In [14], the magnetic wall model was used. Using this model the following wave functions were derived

$$\psi_{TE_{npm}} = J_n\left(\frac{X_{np}}{a}\rho\right)\binom{\sin n\phi}{\cos n\phi}\sin\left[\frac{(2m+1)\pi z}{2d}\right] \tag{28}$$

$$\psi_{TM_{npm}} = J_n\left(\frac{X'_{np}}{a}\rho\right)\binom{\sin n\phi}{\cos n\phi}\sin\left[\frac{(2m+1)\pi z}{2d}\right] \tag{29}$$

where J_n is the Bessel function of the first kind, with $J_n(X_{np}) = 0, J'_n(X'_{np}) = 0, n = 1,2,3,\cdots, p = 1,2,3,\cdots, m = 0,1,2,\cdots$.

From the separation equation $k_\rho^2 + k_z^2 = k^2 = \omega^2\mu\epsilon$, the resonant frequency of the npm mode can be found as follows:

$$f_{npm} = \frac{1}{2\pi a\sqrt{\mu\epsilon}}\sqrt{\begin{Bmatrix} X_{np}^2 \\ X_{np}'^2 \end{Bmatrix} + \left[\frac{\pi a}{2d}(2m+1)\right]^2} \tag{30}$$

From the wave functions, the far-field patterns were also derived. The input impedance could not be derived using the magnetic wall model, so it was studied solely experimentally.

Another cylindrical DRA analysis method was developed using a body of revolution (BOR) analysis [13]. In this method surface integral equations are used to formulate the problem, then the method of moments (MoM) is used to reduce the integral equations to a system of matrix equations [13]. Expressions for resonant frequencies, radiation Q-factor,

26

field patterns, and input impedance are derived for coaxial probe and narrow slot excitation.

Because of the difficulty in calculating resonant frequency and Q-factor for DRA designs, tables and graphs have been created to assist the DRA designer [15]. A procedural design process can be followed using these charts to choose a good DRA design for a given set of specifications. An example of the design charts for the $TE_{01\delta}$ mode is shown below. There has recently been a Matlab program developed to automate much of the DRA design procedure using the approximate solutions discussed above [16]. The authors implemented an analysis and design option so that the user can determine resonant frequency and Q-factor based on a current design or generate DRA dimensions that satisfy the input specifications.
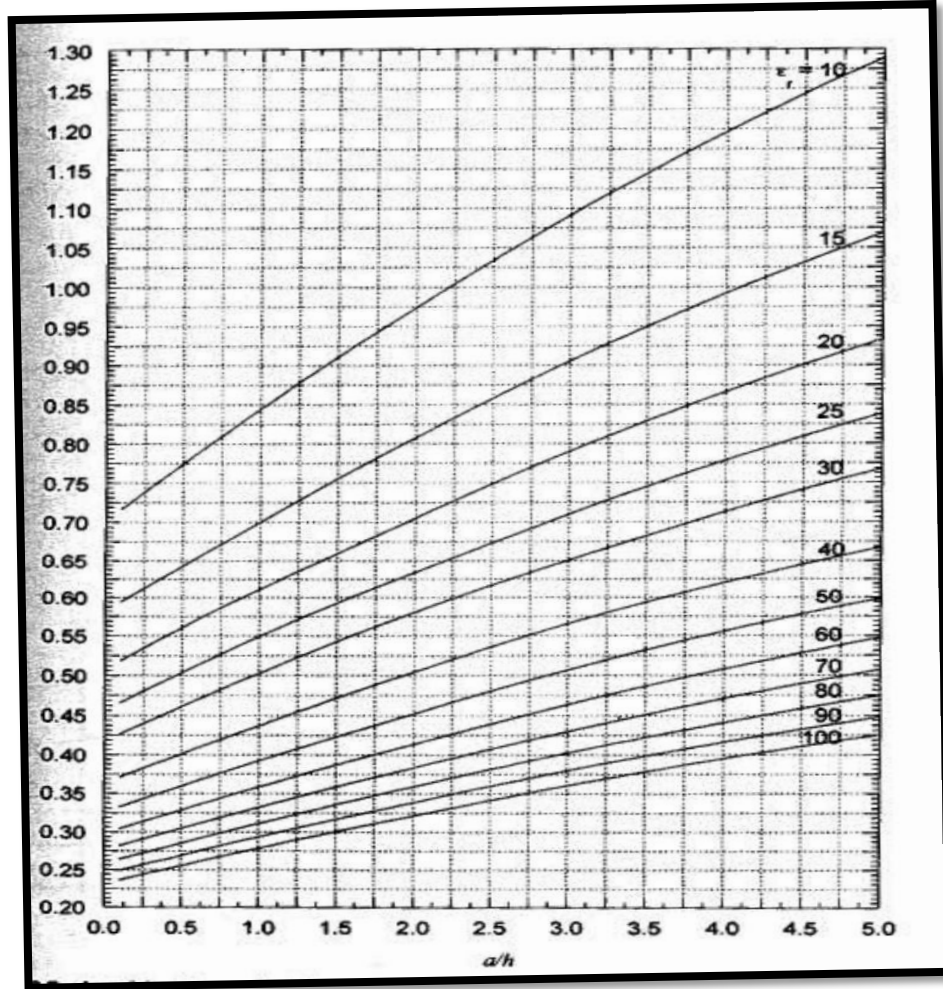
Figure 12: DRA Design Chart [15]

Over the years, much work and many publications have been presented in the area of DRAs. Topics have included feed/coupling techniques, broadband element designs, measurement techniques, DRA arrays including mutual coupling analysis, and novel designs for low frequency and multi-band applications. A select few publications have been chosen from these categories and will be presented in this section.

The feed choice for a DRA is critical as it not only affects the impedance match between the source and the antenna element, but also affects which radiating mode is excited. The most common excitation method is probably that of the single wire or coaxial

probe. This was the method used in [14] and continues to be an efficient way of feeding a DRA element. A drawback to this method at the time was an inability to calculate the input impedance. In [17], a formulation based on BOR and MoM was used to calculate the input impedance of a DRA excited by a coaxial probe. The formulation used thin wire elements which could be interior or exterior to the DRA. The results were verified experimentally and numerically. Due to difficulties in manufacturing a probe fed DRA, microstrip line was considered as a feed method and demonstrated strong coupling around 2-7 GHz [18]. Following this was excitation methods using microstrip line in conjunction with an aperture in the ground plane also known as aperture coupling. Aperture coupling was established as a viable feed technique for a cylindrical DRA at frequencies between 14 and 16 GHz [19]. Another form of aperture coupling was presented using a slotted waveguide as the feed mechanism [20]. In this case, the objective was to actually improve the radiation characteristics of a slotted waveguide by fitting a cylindrical DRA element on top of the slot. The frequency bandwidth of a waveguide slot is relatively low. The authors showed that having the waveguide slot feed a DRA, half-power bandwidth was improved from 13% to approximately 20%.

Improving bandwidth of DRAs has been another popular research topic. The DRA, being a resonant structure has an inherently small bandwidth, but researchers have found ways to greatly improve bandwidth performance. The earliest attempt was in 1989 when Kishk et. al. stacked two different DRAs on top of one another [13]. The two DRAs had different resonant frequencies giving the combined configuration a dual-resonance operation, increasing the antenna bandwidth. A similar method using embedded DRAs

excited by a narrow slot was later explored [21]. Multiple configurations were studied and a bandwidth of over 50% was achieved.

Stacked and embedded DRAs are not ideal due to the difficulty in precise manufacturing. This led to exploration of methods to enhance the bandwidth in single DRAs. One such method was developed by Chair *et. al.* [22]. In this method, a single DRA was excited with two radiating modes with similar characteristics. These two radiating modes were the fundamental $HEM_{11\delta}$ mode and a higher order $HEM_{11\Delta}$ mode. By reducing the radius to height ratio, the higher order mode's resonant frequency was shifted close to the fundamental mode's resonant frequency. Using coaxial and aperture feeds, impedance bandwidths of 26.8% and 23.7% were obtained respectively. Another novel single DRA design for improved bandwidth used a DRA that had been notched out on the bottom and fed using an L-shaped probe [23]. This technique was developed to avoid the difficulties in using stacked DRA configurations and the difficulties in drilling of small diameter holes in the DRA. The notch cut into the DRA leads to performance equivalent to a stacked DRA and the L-shaped probe provided the necessary probe length without having to be inserted into the DRA. An impedance bandwidth of 32% was achieved with this method. In another study, a very large impedance bandwidth of 59.1% was achieved using an intermediate substrate with a microstrip fed slot [24]. A dual-offset feedline was also used to further tune the bandwidth.

The DRA array is another research topic of interest. Due to the myriad of applications requiring a narrow beam-width and high adaptability, DRA arrays are needed.

The concept of DRA arrays is no different than traditional antenna arrays. Array theory is still applied in the same way. There are unique challenges that come with

designing a DRA array such as manufacturability, array feed techniques, and mutual coupling between elements. Many examples of linear and planar DRA arrays can be found in [25]. Some of the more interesting publications have revolved around DRA array fabrication. An eight-by-eight array of rectangular DRAs was successfully fabricated using ceramic steriolithography and performed reasonably well with a gain of 23.1 dBi [26]. Petosa et. al. showed that a DRA array could be created by perforating a dielectric substrate with a lattice of holes [27]. The resulting DRA array was compared to a similar microstrip patch array and showed an improvement in gain and bandwidth.

In order to obtain a directive beam with a DRA array, the elements must be closely spaced. This requirement unfortunately leads to mutual coupling which effects the radiation pattern and element input impedances. The level of mutual coupling depends not only on the spacing between elements, but also on the structure, dimensions and dielectric constant of the DRA elements and the mode of operation [13]. Luk and Leung list several references where studies on DRA element spacing have been done to study the mutual coupling effect [13]. These studies indicate that $\frac{\lambda_0}{2}$ spacing tends to yield the best compromise between low mutual coupling and high directivity. Chair *et. al.* actually did a study comparing the mutual coupling between cylindrical DRAs and circular microstrip patch antennas [28]. They found that the mutual coupling in cylindrical DRAs decreases with a decrease in radius to height ratio and that DRAs have a 2 dB stronger mutual coupling than microstrip patch antennas using a dielectric substrate of equivalent permittivity to that of the DRA.

In addition to the common DRA topics already discussed, there have been several novel applications for DRA technology. One such research topic is that of using a dual-band

DRA for commercial GPS and WLAN applications. This single DRA dual frequency antenna operates at 1.575 GHz with right hand circular polarization for L1 GPS and at 2.45 GHz with vertical polarization, omni-directional radiation pattern for WLAN [29]. An image of this design can be seen below.
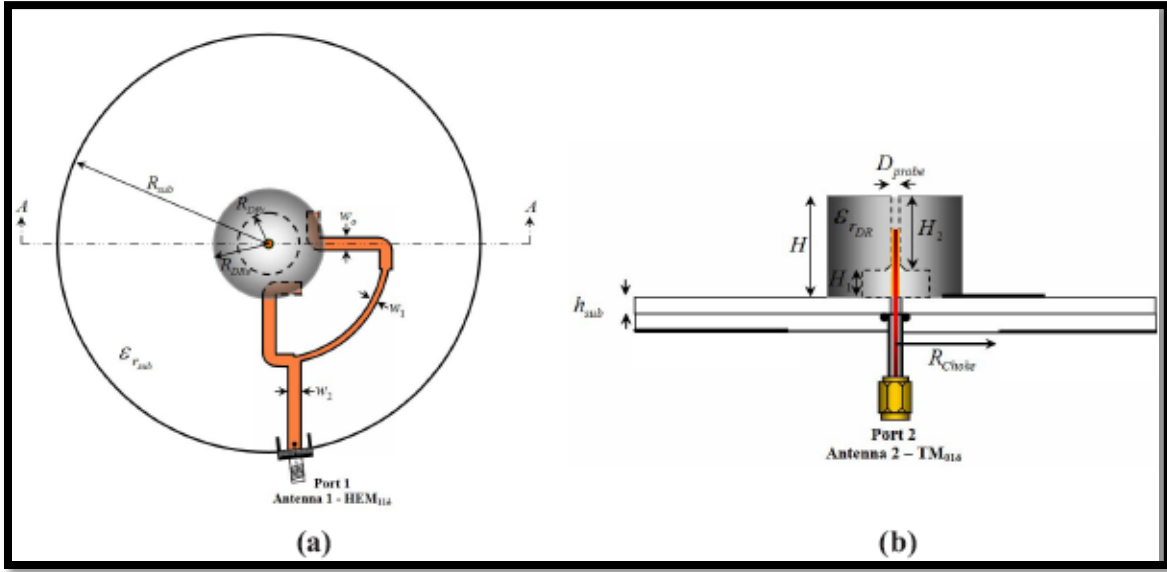

Figure 13: Dual Band DRA for GPS & WLAN Applications [29]

The two ports in this design utilize two different feed probes, which excite the $HEM_{11\delta}$ and $TEM_{01\delta}$ modes providing the necessary hemi-spherical pattern for GPS and omni-directional pattern for WLAN, respectively.

Another recent application for DRA technology has been for low frequency UHF communications or HF VHF radar. This novel design uses liquid as the dielectric for the DRA. A 50 MHz DRA using water as the dielectric was shown to have compact design, low losses, and a high degree of tenability [30]. Water and other similar liquids have a very high dielectric constant with a low loss tangent at low frequencies allowing for small, compact designs. There is also an improvement in manufacturing, as the geometry of liquid DRAs are only limited to the mold shape and size that can be produced. Other

advantages include the absence of air gaps around feeding probes and the ability to completely drain the DRA greatly reducing the radar cross section (RCS).

TRANSMISSION LINE THEORY

The design of a simple antenna feed or a complex feed network requires a solid understanding of transmission line theory. The transmission line can take on many forms such as waveguide, coaxial line, microstrip, stripline, or coplanar waveguide. All of these achieve the same goal of delivering electromagnetic energy from a source to a destination. Difficulties arise when there are discontinuities in the transmission line. This could be due to a transition between two different types of transmission lines i.e. microstrip to coaxial, or an abrupt change in transmission line dimension. These challenges will be discussed in further detail following a general overview of transmission line theory.

Transmission line theory bridges the gap between field analysis and basic circuit theory [4]. Basic circuit analysis uses a lumped element circuit model, as it assumes that the physical extent of the network is much smaller than the electrical wavelength. Transmission line theory is applied when the transmission line length is a fraction of the wavelength or several wavelengths long. It is called a distributed network, because voltages and currents can vary in magnitude and phase over its length. Using a lumped element circuit model, the wave propagation characteristics can be derived for a transmission line in terms of voltage, current, and characteristic impedance of the line.

Consider the two-wire transmission line shown in Figure 14. The two-wire model is used due to a transmission line always having at least two conductors.
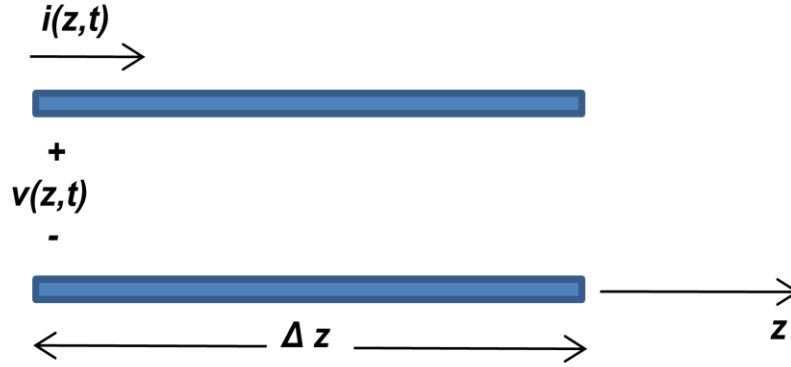
Figure 14: Two-Wire Transmission Line

This piece of transmission line can be modeled as a lumped-element circuit as shown in Figure 15, where R is the series resistance per unit length, L is the series inductance per unit length, G is the shunt conductance per unit length, and C is the shunt capacitance per unit length. This model represents an infinitesimal length of transmission line, but a finite length transmission line could be modeled by cascading several of these sections together.
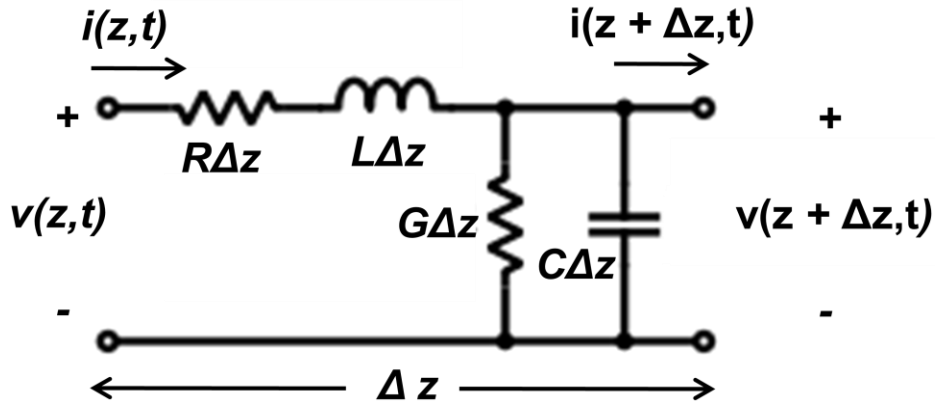

Figure 15: Lumped-Element Equivalent Circuit

From this circuit, Kirchoff's voltage law can be applied to give

$$v(z,t) - R\Delta z i(z,t) - L\Delta z \frac{\delta i(z,t)}{\delta t} - v(z+\Delta z, t) = 0 \tag{31}$$

35

Kirchoff's current law is used to yield

$$i(z,t) - G\Delta z v(z + \Delta z, t) - C\Delta z \frac{\delta v(z + \Delta z, t)}{\delta t} - i(z + \Delta z, t) = 0 \qquad (32)$$

Dividing these two equations by Δz and taking the limit as $\Delta z \to 0$ gives the following differential equations:

$$\frac{\delta v(z,t)}{\delta z} = -Ri(z,t) - L\frac{\delta i(z,t)}{\delta t} \qquad (33)$$

$$\frac{\delta i(z,t)}{\delta z} = -Gv(z,t) - C\frac{\delta v(z,t)}{\delta t} \qquad (34)$$

These equations referred to as the telegrapher equations, giving a time-domain representation of the transmission line. For the sinusoidal steady-state condition, with cosine-based phasors, these equations simplify to

$$\frac{dV(z)}{dz} = -(R + j\omega L)I(z) \qquad (35)$$

$$\frac{dI(z)}{dz} = -(G + j\omega C)V(z) \qquad (36)$$

Using these equations, wave equations can be found for the transmission line

$$\frac{d^2V(z)}{dz^2} - \gamma^2 V(z) = 0 \qquad (37)$$

$$\frac{d^2I(z)}{dz^2} - \gamma^2 I(z) = 0 \qquad (38)$$

where

$$\gamma = \alpha + j\beta = \sqrt{(R + j\omega L)(G + j\omega C)} \qquad (39)$$

is the complex propagation constant. Traveling wave solutions to (37) and (38) can be found as

$$V(z) = V_0^+ e^{-\gamma z} - V_0^- e^{\gamma z} \qquad (40)$$

36

$$I(z) = I_0^+ e^{-\gamma z} + I_0^- e^{\gamma z} \tag{41}$$

where $e^{-\gamma z}$ represents wave propagation in the $+z$ direction, and $e^{\gamma z}$ represents wave propagation in the $-z$ direction. The current on the line can be found by applying equation (35) to equation (40).

$$I(z) = \frac{\gamma}{R + j\omega L} [V_0^+ e^{-\gamma z} - V_0^- e^{\gamma z}] \tag{42}$$

Comparison with (41) shows that a characteristic impedance, Z_0, can be defined as

$$Z_0 = \frac{R + j\omega L}{\gamma} = \sqrt{\frac{R + j\omega L}{G + j\omega C}} \tag{43}$$

which relates the voltage and the current on the line as

$$\frac{V_0^+}{I_0^+} = Z_0 = -\frac{V_0^-}{I_0^-} \tag{44}$$

Using this derived expression for Z_0, equation (41) can be rewritten as

$$I(z) = \frac{V_0^+}{Z_0} e^{-\gamma z} - \frac{V_0^-}{Z_0} e^{\gamma z} \tag{45}$$

This equation can then be converted back into the time domain and expressions for wavelength, λ, and phase velocity, v_p, can be found as

$$\lambda = \frac{2\pi}{\beta} \tag{46}$$

$$v_p = \frac{\omega}{\beta} = \lambda f \tag{47}$$

The equations derived above are for the general lossy transmission line. Often times, a transmission line can be considered lossless and these expressions are greatly simplified.

To understand how a transmission line is affected by a load, consider the terminated lossless transmission line shown below. Using this circuit, an expression for the reflection coefficient, Γ will be derived. A reflection will occur if there is a mismatch between the characteristic impedance Z_0 and the load impedance Z_L. The total voltage on the line can be written as a sum of incident and reflected waves.

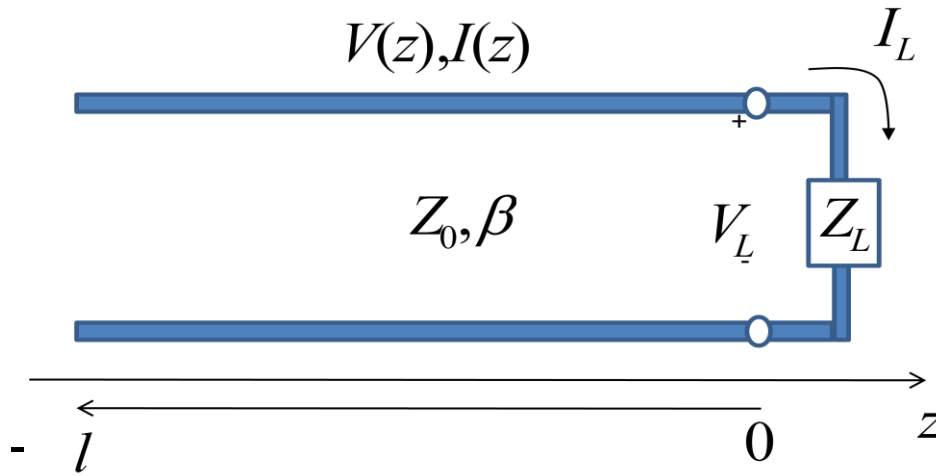$$V(z) = V_0^+ e^{-j\beta z} + V_0^- e^{j\beta z} \tag{48}$$

Figure 16: Lossless Terminated Transmission Line

The total current on the line can likewise be written as

$$I(z) = \frac{V_0^+}{Z_0} e^{-j\beta z} - \frac{V_0^-}{Z_0} e^{j\beta z} \tag{49}$$

The total voltage and current are related by the load impedance, so at $z = 0$ we have

$$Z_L = \frac{V(0)}{I(0)} = \frac{V_0^+ + V_0^-}{V_0^+ - V_0^-} Z_0 \tag{50}$$

Solving this for V_0^- yields

$$V_0^- = \frac{Z_L - Z_0}{Z_L + Z_0} V_0^+ \tag{51}$$

38

The amplitude of the reflected wave divided by the amplitude of the incident wave is the voltage reflection coefficient.

$$\Gamma = \frac{V_0^-}{V_0^+} = \frac{Z_L - Z_0}{Z_L + Z_0} \tag{52}$$

The total voltage and current can now be written in terms of the reflection coefficient, Γ.

$$V(z) = V_0^+ \left[e^{-j\beta z} + \Gamma e^{j\beta z} \right] \tag{53}$$

$$I(z) = \frac{V_0^+}{Z_0} \left[e^{-j\beta z} - \Gamma e^{j\beta z} \right] \tag{54}$$

A transmission line impedance equation can be derived giving the impedance seen looking into the line, which happens to vary with position. The final form of this equation is shown below.

$$Z_{in} = Z_0 \frac{Z_L + jZ_0 \tan \beta l}{Z_0 + jZ_L \tan \beta l} \tag{55}$$

Another important term used in the design of transmission lines is return loss, RL. This term describes the loss of power in dB due to a mismatched load and is given as

$$RL = -20 \log|\Gamma| \text{ dB} \tag{56}$$

There are also special cases of lossless terminated transmission lines. For instance, if the load were replaced with a short circuit then the input impedance seen looking into the line would be purely reactive. Likewise, if the load were replaced with an open circuit it also would be purely reactive. Typically, these short or open transmission lines are used as stubs in RF circuits for tuning. The most important special property as it applies to the design of an antenna feed network is that of the quarter-wave transformer. A transmission line of characteristic impedance Z_0 can be matched to a load resistance R_L by inserting a

section of transmission line with length equal to a quarter-wavelength and characteristic impedance Z_1. Doing so makes the reflection coefficient, Γ, looking into the $\frac{\lambda}{4}$ matching section equal to zero. To achieve this, the input impedance seen looking into the $\frac{\lambda}{4}$ section is found as

$$Z_{in} = Z_1 \frac{R_L + jZ_1 \tan \beta l}{Z_1 + jR_L \tan \beta l} \tag{57}$$

Inserting $\frac{\lambda}{4}$ for l and performing some algebraic manipulation, the input impedance is reduced to

$$Z_{in} = \frac{Z_1^2}{R_L} \tag{58}$$

To make $\Gamma = 0$, it is required that $Z_{in} = Z_0$, which yields the expression for the characteristic impedance of the quarter-wave matching section.

$$Z_1 = \sqrt{Z_0 R_L} \tag{59}$$

The quarter-wave transformer is a very practical solution to matching two transmission lines of different characteristic impedances and is commonly used in feed networks.

TRANSMISSION LINE DISCONTINUITIES

Virtually all practical distributed circuits, no matter the type, must inherently contain discontinuities [31]. Common applications of transmission line circuits such as amplifiers, filters, phase shifters, and antenna feed networks require many transitions, bends, curves, width changes, etc., leading to discontinuities. An engineer must take careful

consideration when designing such a device to minimize losses and inefficiencies due to these discontinuities. Discontinuities and junctions denote any change in the cross-section of a straight waveguiding structure [32]. Discontinuities or junctions can create inductive and capacitive effects and also cause losses due to radiation. At low frequencies these effects may be negligible, but at higher frequencies, 10 GHz and above, these effects become quite significant. There are some calculation methods for analyzing very simple transmission line discontinuities, but most require thorough field analysis techniques using Maxwell's equations [32].

Examples of commonly encountered discontinuities are series coupling gaps, short circuits through to the ground plane, right-angled corners or bends, curves, step width changes, tapers, T-junction, or cross-junctions [31-32]. A few of these as they apply to miscrostrip will briefly be discussed.

Short circuits are often needed to ground a structure or to transition from one layer of a printed-circuit board (PCB) to another. At low frequencies, a short thin wire can be used for this purpose with negligible reactive effects. At higher frequencies, > 3 GHz, reactance is significant and must be dealt with. Typically through holes are drilled from the microstrip line to the ground plane and are metallized around their cylindrical surfaces. This technique, along with choosing a proper hole diameter dependent upon strip width can provide a practically frequency independent reactance, which is beneficial in any broadband design [31].

Right-angled bends are particularly lossy. Capacitance arises due to the additional charge accumulation at the corners and inductances are caused by current flow interruption. Most of the current flows in the outer edges of the microstrip, so inductance

is considerable at the outer corner. Chamfered or mitered bends, along with curves (radial bends) are compensation techniques used to reduce the unwanted capacitances and inductances in right-angled bends. Moment methods and other numerical techniques have been used for determining what form the miters or curves should take to produce appropriate inductances and capacitances [31].

Step width changes are techniques used to match two or more different width microstrip lines. The most common of these techniques is the quarter-wave transformer which has already been described. More sophisticated techniques use multiple gradually increasing or decreasing step widths. This can increase the bandwidth over which the transformation is acceptable. Tapering is a special case of a stepped transformer where the number of steps approaches infinity leading to the smooth taper of the transmission line.

T-junctions are used quite frequently in a variety of microwave circuits, especially feed networks. Capacitances and inductances occur at the junction point of this circuit. One compensation method is to introduce a slit across the width of the main-through microstrip line [31]. Other forms of compensation modify the microstrip lines in the vicinity of the junction in order to compensate for reference plane shifts.

DRA ARRAY DESIGN AND SIMULATION

SINGLE ELEMENT DESIGN

A starting point for any antenna array design should be the design and modeling of a single element. As discussed in the array theory section, the radiation pattern of an array is dependent upon the radiation pattern of each individual element. Because of the lack of analytic solutions to a cylindrical DRA, charts of numerically modeled designs or tables of pre-simulated designs are usually a good starting point for a design that will be later optimized. Ideally, one would design for optimum gain, bandwidth, and efficiency without concern for the resulting element dimensions, dielectric properties, or feeding method. For this research however, the goal was to design a practical DRA array that could be easily manufactured with repeatability. Some design properties such as those mentioned above must be restricted due to cost, availability, or ease of manufacturing. One such restriction encountered early on was height of the DRA. The method chosen for fabrication of the DRA array, which will later be discussed in detail, requires a planar sheet of dielectric material. After research and discussions with several laminate providers, it was found that the maximum thickness high dielectric constant material that could be fabricated was roughly 5 mm at the time of this research. The starting parameters for the 9.75 GHz single DRA design were ultimately chosen using a combination of previous simulations performed by

Chair, et. al. [28] and the design charts from [15]. These parameters are denoted in the table below.

Table 2: Initial DRA Parameters

Design Parameter	Initial
Element Height	5.00 mm
Element Radius	3.00 mm
Probe Height (Inside Element)	2.00 mm
Probe Radius	0.31 mm
Probe Offset Percentage (from Center of Element)	70%

For DRA simulation and optimization, the High Frequency Structure Simulator (HFSS) software from Ansoft Corporation [33] is used. HFSS incorporates a broad range of material properties when creating a model, including the ability to create custom material properties. This is crucial as the material properties governing DRA performance such as permittivity, conductivity, and loss tangent are all available for customization. HFSS is also an ideal tool for simulating complex geometries potentially affording enhanced bandwidth and tuning of the resonant mode. HFSS uses a full wave Finite Element Method (FEM) to solve for the electric and magnetic fields across the problem domain. HFSS's parametric and optimization tools make it perfect for the design of electromagnetically sensitive geometry such as the DRA.

A cylindrical DRA was modeled in HFSS using the parameters from Table 2.   A 125 mil thick sheet of aluminum was used as the ground plane. An aluminum ground plane of this thickness was chosen to provide rigidity for a large array and to provide a flat surface to mount to the feed network. The feed mechanism chosen is a coaxial feed composed of a silver center conductor with an air filled dielectric.   The dielectric substrate is AD1000 form Arlon microwave materials and has a dielectric constant, $\epsilon_r = 10.2$. To excite the DRA a wave port was defined on the bottom surface of the coaxial line. HFSS assumes that each wave port you define is connected to a semi-infinitely long waveguide that has the same cross-section and material properties as the port. When solving for the S-parameters, HFSS assumes that the structure is excited by the natural field patterns (modes) associated with these cross-sections. The 2D field solutions generated for each wave port serve as boundary conditions at those ports for the 3D problem. A labeled profile view of the single DRA model drawn in HFSS is shown in Figure 17.

An air box is placed around the DRA sized to be $\frac{\lambda}{2}$ from the center of the DRA. The default boundary for all objects modeled in HFSS is perfect electrical conductor (PEC). In order to solve for the far-field radiation pattern of the radiating element, a perfectly matched layer (PML) boundary condition was defined on the five surfaces surrounding the DRA. PML is a fictitious material that fully absorbs the electromagnetic field impinging upon it. The bottom surface was left as default PEC. For all designs, the variables of interest were parameterized so that they could easily be swept or optimized as needed.
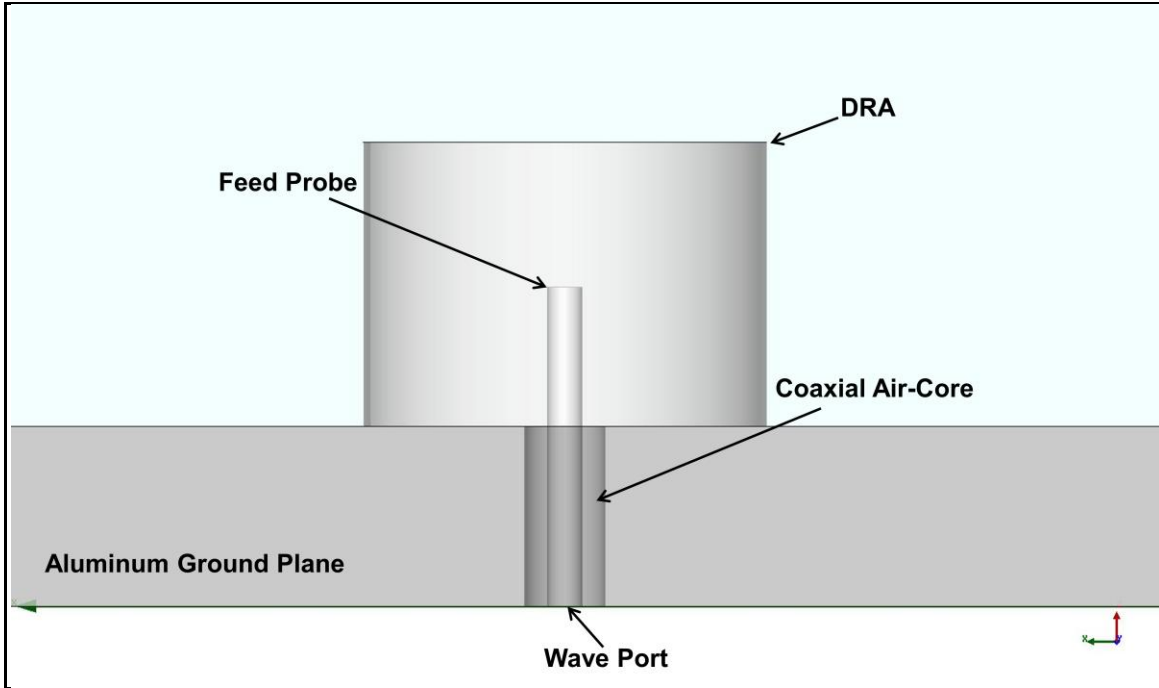
Figure 17: Single DRA HFSS Model

The simulation process went as follows. To achieve the best results from an optimization and to reduce simulation time, it is best to have a good initial guess for the design parameters being optimized. This was done by performing a separate parametric study for each parameter; DRA radius, probe height, and probe offset position. Using the initial values in Table 2 for probe height and probe offset percentage, the DRA radius was swept from 2.0 to 7.0 mm in 0.5 mm steps. The reflection coefficient at the input port, S_{11}, was plotted for each iteration. The solution is solved for only at the center frequency of 9.75 GHz. This insures that the values being fed to the optimization routine are values which should minimize reflections at the desired resonant frequency.
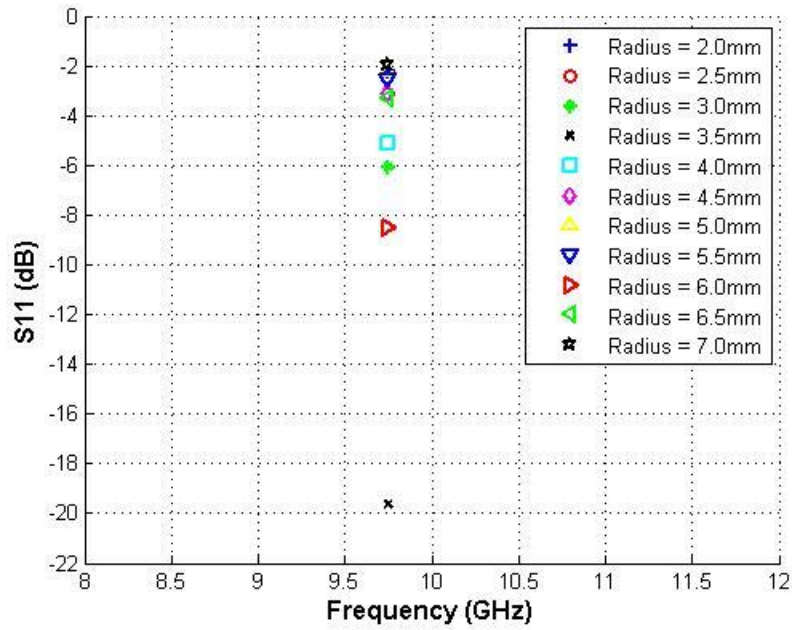
Figure 18: DRA Radius Parametric Analysis

Parametric analyses were done in the same way for the probe height and probe offset. In each case, the values of the two parameters not being swept were set to the initial values from Table 2. The parameter value for each run with the lowest S_{11} was chosen as the inputs to the optimization.
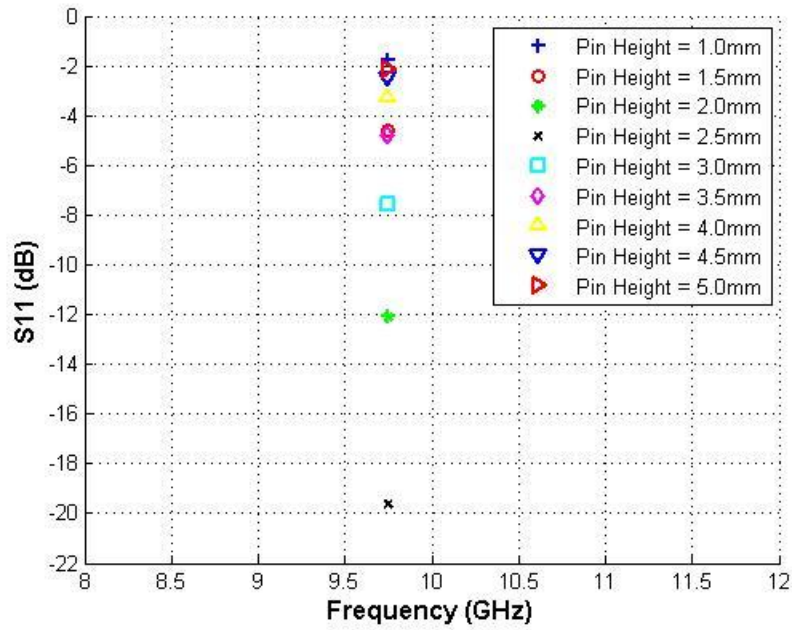
47

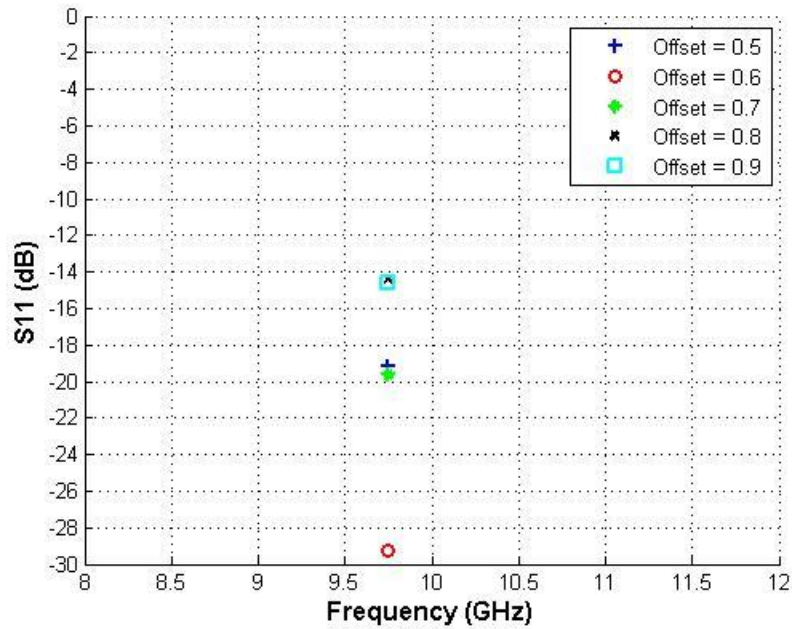**Figure 19: Probe Height Parametric Analysis**

Figure 20: Probe Offset Parametric Analysis

The HFSS optimization was set up to minimize S_{11} across the frequency band. Minimum and maximum values along with minimum step sizes were defined to reduce

48

simulation time and avoid unrealistic results. The results of the optimization gave the following values, DRA radius= 3.55283 mm, offset percentage = 0.59641, and probe height = 2.446742 mm. Since the precision of these results are beyond fabrication tolerances, the values were rounded. The figure below shows S_{11} plotted for the optimized results and the rounded results. The impedance bandwidth of the optimized design (S_{11} < -10dB) is 890 MHz.

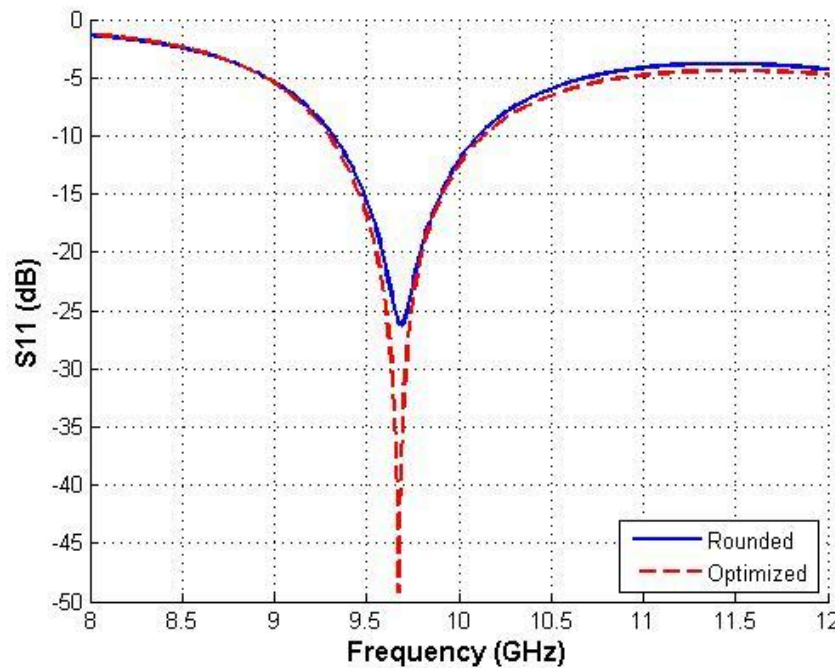**Figure 21: Single DRA Optimization**

4X4 ARRAY DESIGN

Before attempting the design of a large DRA array, a 16 element array was developed. The smaller array would be easier to simulate in HFSS due to the smaller physical size and also easier to fabricate for initial proof of concept. The main goal of simulating the 4x4 array in HFSS was to study mutual coupling effects. Based on traditional array theory, a half-wavelength element spacing would produce an optimal

49

beam pattern. At 10 GHz this would be a spacing of 15 mm. A 4x4 square lattice DRA array was modeled in HFSS with the element spacing parameterized. Again PML boundary conditions were used and the distance from the outer elements to the outside boundaries were set to equal the element spacing value.
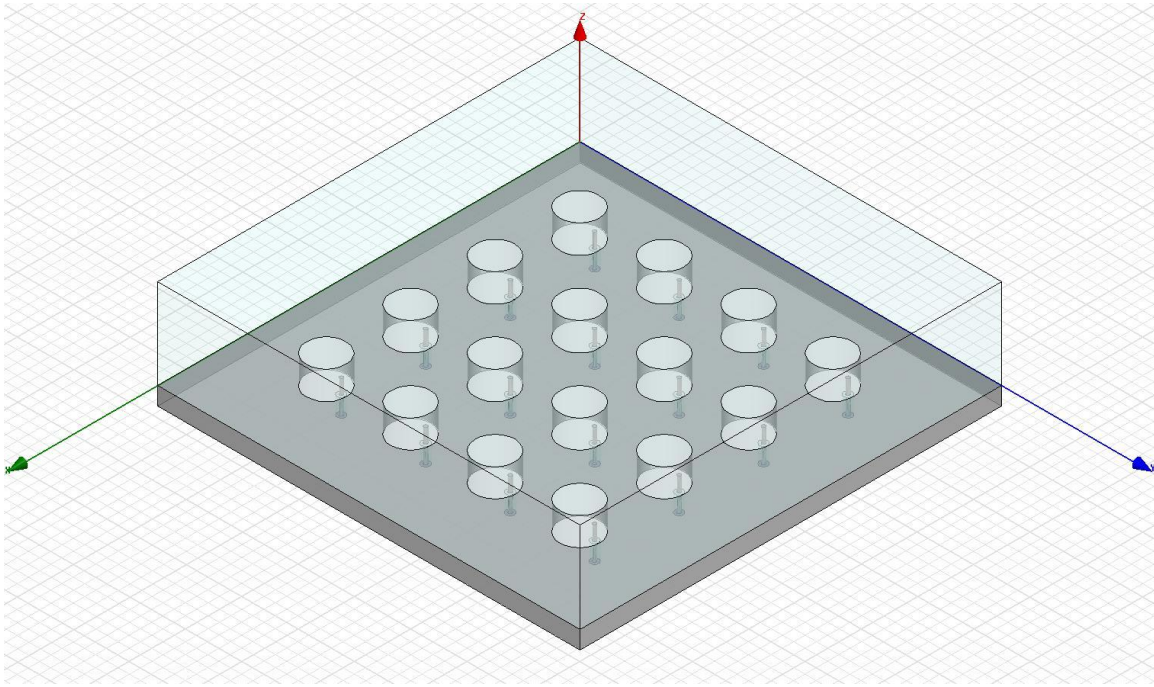

Figure 22: 4x4 DRA Array

The simulation was run at 9.75 GHz with element spacings equal to 15 mm, 15.4 mm, 15.8 mm, 16 mm, 16.2 mm, and 16.5 mm. Due to the symmetry of the design, the far-field pattern was plotted for $\phi = 0$ over all values of θ. This allows one to compare both the gain and sidelobe suppression for each elemental spacing. The results of Figure 23 show that although an element spacing of 15 mm does not offer the highest gain, it does have the best sidelobe suppression. Antenna design is all about tradeoffs and in this case a less than 1 dB smaller gain is being sacrificed for a 2-4 dB sidelobe improvement.
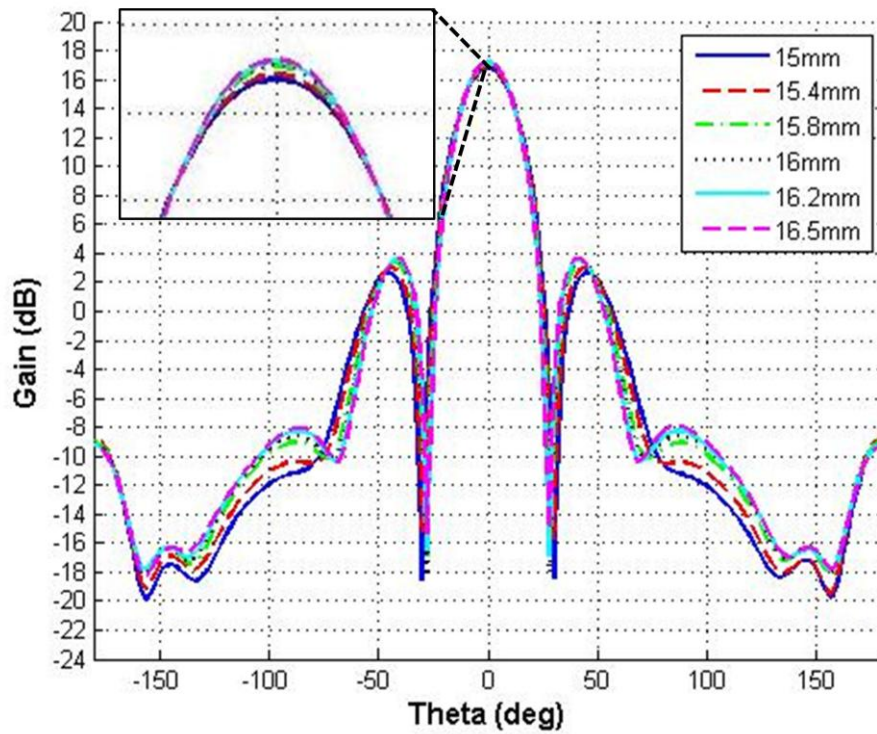
Figure 23: 4x4 DRA Array Element Spacing

The same simulation was also run at 10 GHz for comparison. The radiation pattern was almost identical as that at 9.75 GHz. The reason for this most likely being the effects of the mutual coupling changing the impedance characteristics of the radiating elements, thus changing the impedance bandwidth from that seen in the single DRA design. To further investigate the effect of operating frequency on radiation pattern, another simulation was run from 9 to 10 GHz in 200 MHz steps with a constant element spacing of 15 mm. The results show that from 10 to 9.6 GHz, the radiation pattern is changed little, but the drop off from 10 GHz to 9 GHz is about 3 dB or half power.
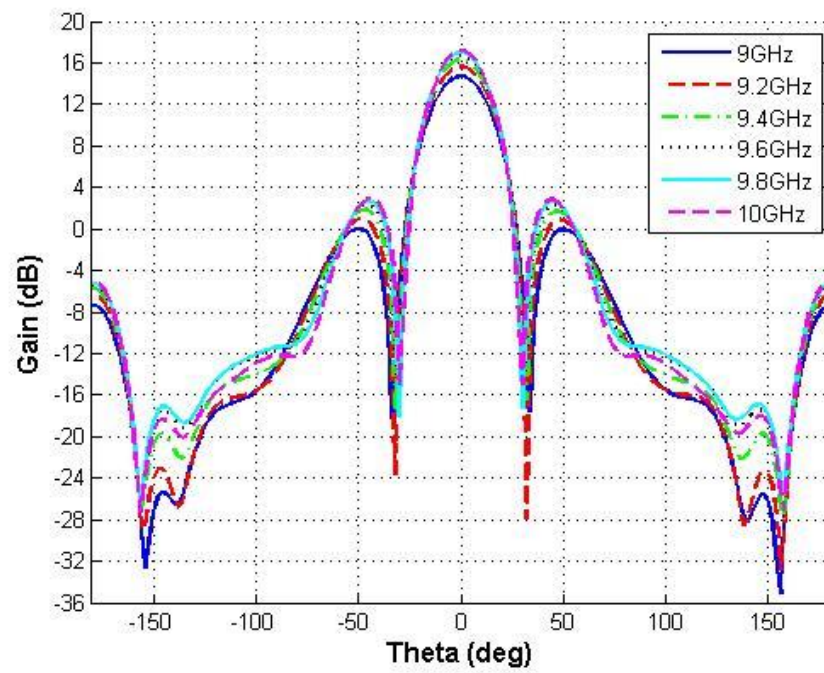
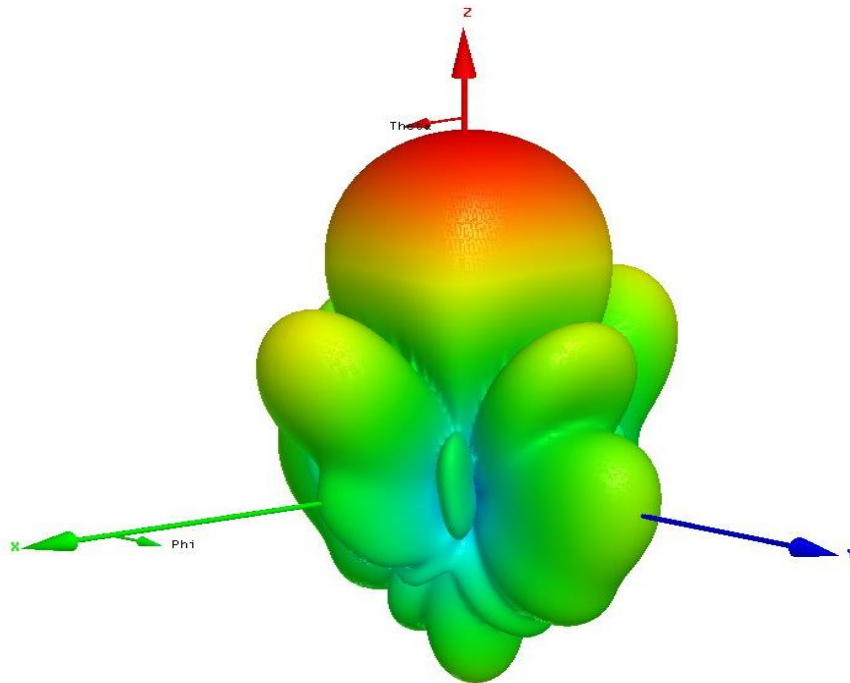**Figure 24: 4x4 DRA Array Frequency Sweep (15 mm spacing)**

Figure 25: 4x4 DRA 3D Radiation Pattern

16X16 ARRAY DESIGN

Simulation of a full 16x16 DRA array in HFSS is unreasonable for current hardware. The number of tetrahedra used to model a complex geometry of this size at x-band frequencies would require upwards of 64 GB of memory and an extremely fast processor to solve in a reasonable time. HFSS does provide other methods of solving large antenna arrays. The trivial solution would be to solve for a single DRA and use the array factor post processing option to visualize the radiation pattern of an n-element array at a desired inter-element spacing. This method would provide an ideal solution that assumes absolutely no mutual coupling between elements. Another method makes use of master and slave boundary conditions. Master and slave boundaries allow one to model planes of periodicity where every point on the slave boundary surface is forced to match the electric field of every corresponding point on the master boundary surface to within a phase difference. The master and slave boundaries simulate an infinite array, which is valid for arrays that are 10x10 and larger as a rule of thumb. Some assumptions that are made are every element pattern of each element is identical and no edge effects are included. The master and slave boundaries do incorporate mutual coupling from every element, which gives a much more accurate solution than simply applying the array factor to a single element. Essentially, the master and slave boundary condition is an infinite array simulation used to approximately solve a finite array.

The optimized single DRA design was used as a starting point for the 16x16 array simulation. The outer boundaries were changed from PML to master and slave boundaries while the top layer remained PML. When assigning the master boundary, a reference u-v coordinate system must be define as seen in the following figure. The u vector is defined

on the lower left face of the DRA air box with a positive z direction. The v vector is automatically set to be orthogonal to the u vector. This coordinate system is used when mapping the E-field from the master to the slave boundary.
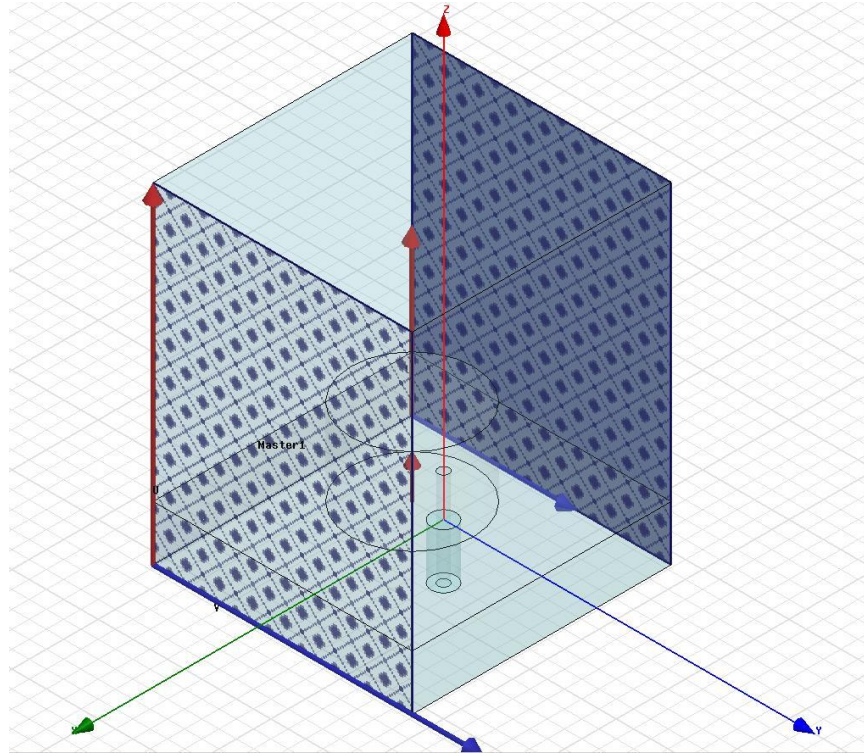

Figure 26: Master/Slave DRA Model

Simulations were run for several different element to element spacings to determine the effects of mutual coupling for a large array. S_{11} was plotted for several of these spacings including the optimum element spacing of 15 mm, which was also the optimum spacing for the 4x4 array. An important note is that the plot represents the port reflection of a single DRA element in an infinite array. This would be equivalent to one of the central elements of a 16x16 array. The outer elements, however, would have a different reflection coefficient at their source port due to the change in mutual coupling from that of the central elements. The plot still gives very good insight into the effects of mutual coupling which is the desire.
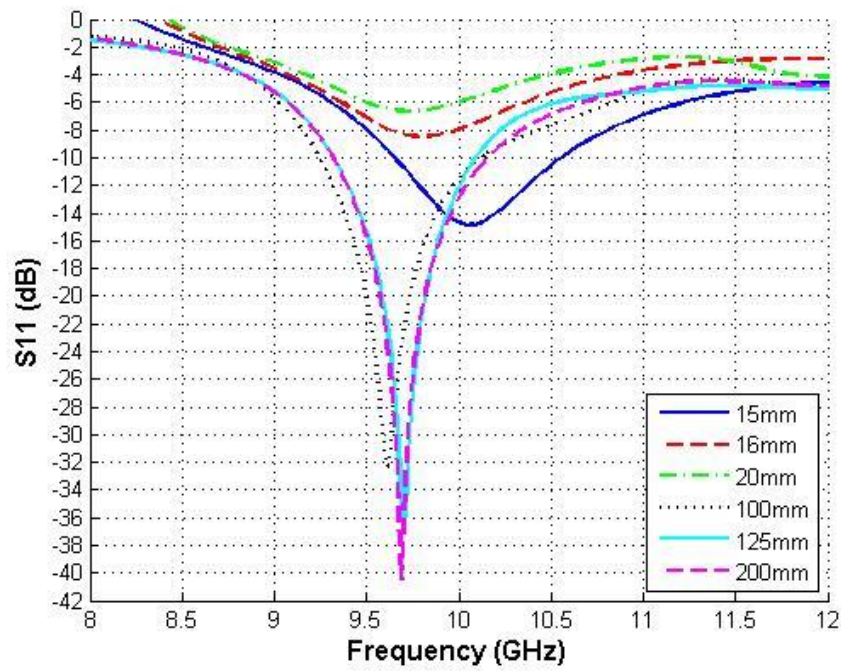
Figure 27: 16x16 Array S_11 Comparison

It is clear from this plot that element spacing has a large effect on resonant frequency. At 15 mm the resonant frequency is approximately 10 GHz with good bandwidth. As spacing is increased the resonant frequency is shifted down. The spacings of 100 mm, 125 mm, and 200 mm were chosen to show at what spacing mutual coupling is negligible. At 125 mm, the spacing in which mutual coupling is no longer a consideration is clearly not practical for antenna array design, so mutual coupling must be accounted for.
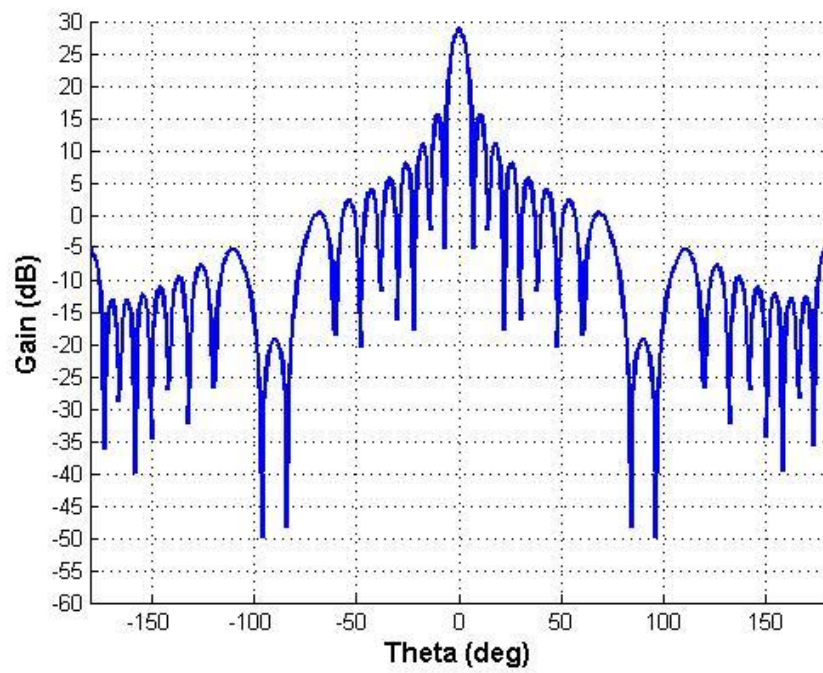
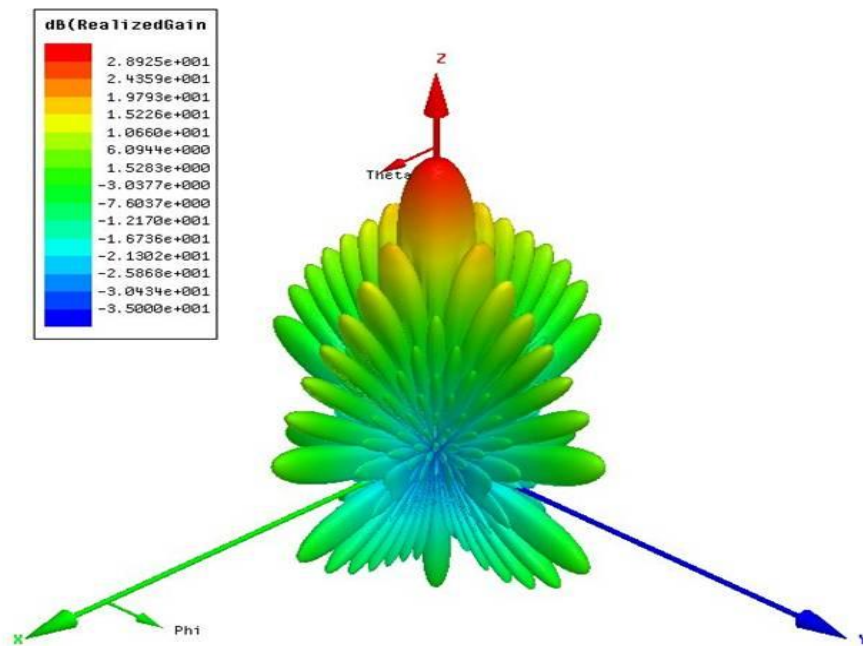**Figure 28: 16x16 Array Radiation Pattern (Φ=0)**

Figure 29: 16x16 Array 3D Pattern

Figure 28 and Figure 29 show the radiation pattern of the 16x16 DRA array with 15 mm spacing at 10 GHz. The radiation pattern was generated using the array factor. The single element pattern used by the array factor calculation includes the mutual coupling effects from the master and slave boundary setup, so it represents a more accurate solution. In the $\phi = 0$ plot, it is seen that the main lobe gain is ~29 dB and the nearest sidelobes are 14 dB down. The 3D pattern is scaled in magnitude to show all of the side and rear lobes. The majority of these lobes are 30 dB down or more from the main lobe.

Being content with this design for a 16x16 DRA array, the table of parameters is updated with the optimized results from both the single DRA simulations and the array simulations.

Table 3: Final DRA Parameters

Design Parameter	Initial	Final
Element Height	5.00 mm	5.00 mm
Element Radius	3.00 mm	3.55 mm
Probe Height (Inside Element)	2.00 mm	2.45 mm
Probe Radius	0.31 mm	0.31 mm
Probe Offset Percentage (from Center of Element)	70%	60%
Element Spacing	N/A	15 mm

FEED NETWORK DESIGN AND SIMULATION

The DRA simulations previously discussed excluded a critical design element necessary for any antenna array, the feed network. The feed network is simply the mechanism used to deliver energy from a source to each antenna element. Design of a successful feed network utilizes the transmission line techniques discussed in Chapter 3. The effects of the feed network on antenna performance increase as a function of array size. For a small 4x4 array, the feed losses of the feed network may not be crucial, but as the array size is increased so are line lengths, number of transitions, and number of element excitation points. Literature regarding the design of efficient wide bandwidth feed networks is limited. Most feed network literature is focused on either microstrip patch arrays or general arrays, which are both still relevant to DRAs as the majority of the feed network remains the same between a patch antenna array and a DRA array [34-36]. The process to design a low loss wide-band feed network is discussed below.

OPTIMIZATION OF FEED NETWORK TRANSITIONS

A corporate feed equal distribution network was chosen for this design because of its significant bandwidth advantage over a serial feed network. Scenarios such as power junctions and impedance mismatches must be carefully considered in the design of the feed

network as they can have a major impact on overall antenna performance. The two primary loss factors of any transmission line circuit at x-band frequencies are impedance mismatches which commonly occur at power junctions in feed networks, and radiation losses which are innate to microstrip technology and can be avoided by minimizing transmission line length. Using Ansoft Designer software, the DRA corporate feed network was examined and modified for improved bandwidth performance and losses. Ansoft Designer uses a 2.5D Method of Moments (MoM) solver to quickly and accurately solve planar electromagnetic problems. The original feed network was generated using a software routine developed by Radiance Technologies, Inc.. The software accepts frequency, dielectric constant, and array size as inputs and generates a .DXF drawing file of the corporate feed network. The generated feed network is composed of standard T power dividers and quarter-wave transformers for impedance matching. An example of a 4x4 array generated with this software can be seen below.

This design uses quarter-wave transformers where there is space and uses 'hard' transitions everywhere else. 'Hard' transitions are those in which two unequal widths of transmission line are connected with no transformation section between them. This creates a bad mismatch and much of the incident power will be reflected. Before trying to improve upon the design, it is first important to show the true effects of these 'hard' transitions as more branches are added.
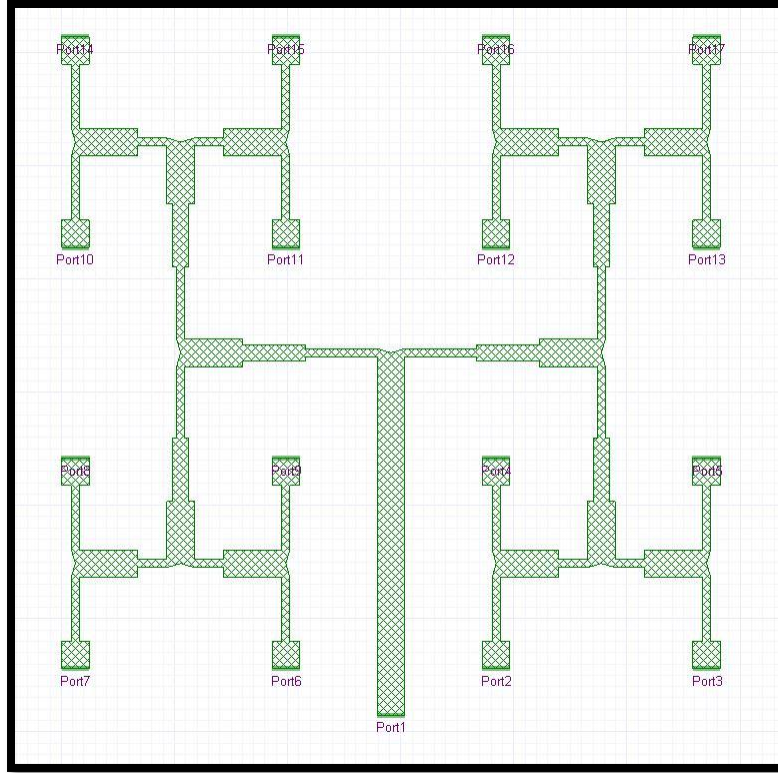
Figure 30: Initial 4x4 Feed Network

The feed network was simulated in 3, 5, and 8 port sections in order to see the effect of adding additional branches to the feed. S-parameter data is reported for each case where S_{11} represents the reflection at the input of the feed network. Transmission S-parameter data is also reported for arbitrarily chosen output ports. The first simulation of the 3 port subsection is essentially a standard T power divider network. There are no 'hard' transitions in this design due to the quarter-wave transformers being used. The Designer model and the simulation results are shown in Figure 31. Resonance for this structure is ~10.2 GHz with a wide bandwidth covering all of x-band. Both S_{21} and S_{31} are slightly less than -3 dB, which is expected for a 2 way power divider.
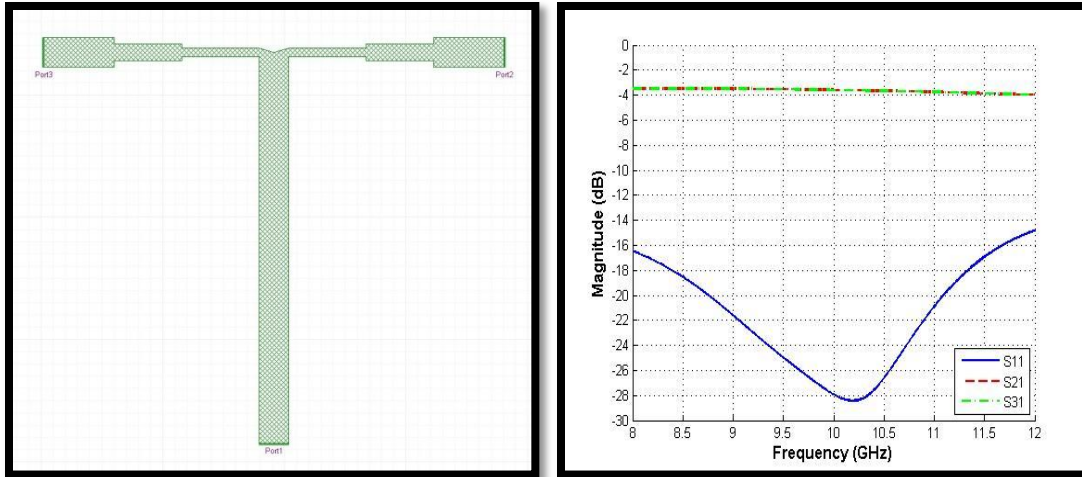
Figure 31: (a) 3 Port Subsection (b) 3 Port S-Parameter Data

As the feed network is expanded into 5, 8, and 16 port sections the effects of discontinuities are more apparent. Shown below are the physical layouts and simulation results for the remaining subsections and the fully constructed 4x4 feed network.
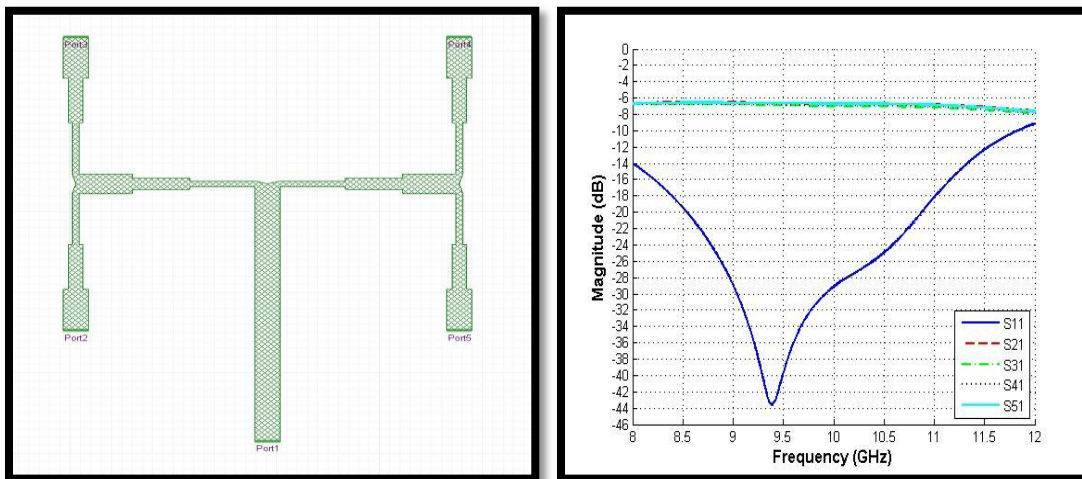

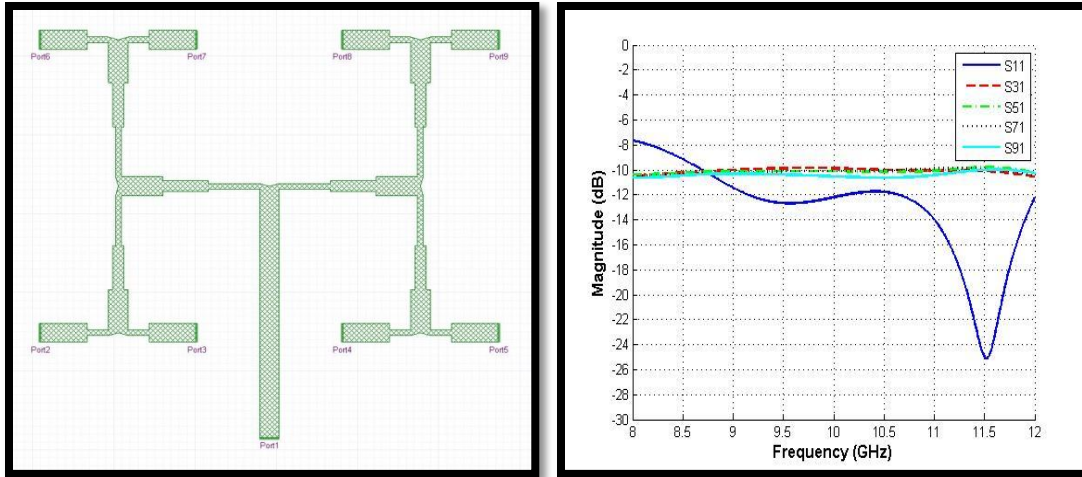**Figure 32: (a) 5 Port Subsection (b) 5 Port S-Parameter Data**

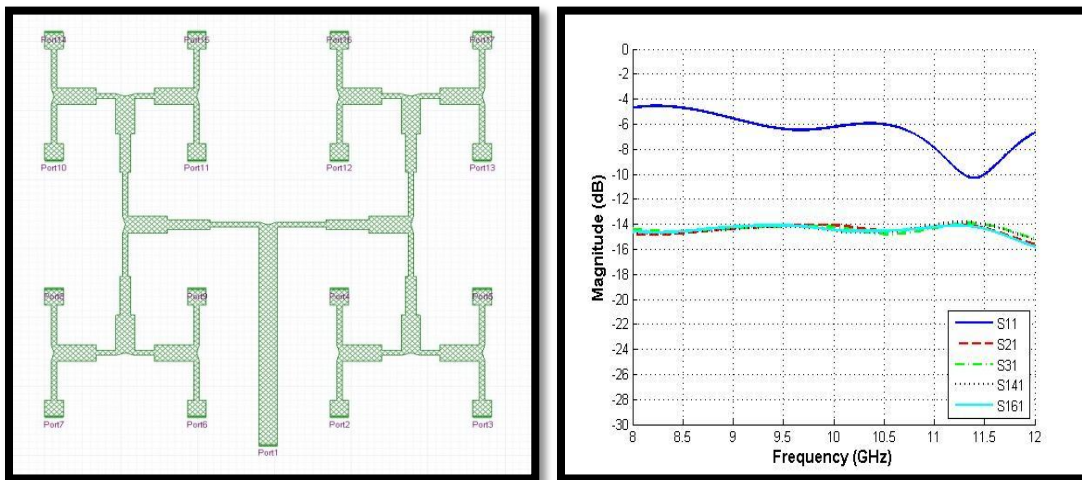**Figure 33: (a) 8 Port Subsection (b) 8 Port S-Parameter Data**

Figure 34: (a) 16 Port Subsection (b) 16 Port S-Parameter Data

The 5 port subsection is similar to the 3 port subsection and has a shifted resonance at 9.4 GHz. There does seem to be some degradation at the outer frequencies of the band, but nothing significant. The bandwidth is still excellent over x-band. As the feed network is expanded to the 8 port subsection, the performance significantly worsens. The resonance has been shifted to 11.5 GHz, and the overall bandwidth is greatly reduced. Looking at the layout for the 8 port subsection, notice that this is the first layout that introduces 'hard' transitions prior to the output ports. This is the only major difference from the other

subsections other than path length from input to outputs, so it is reasoned that these 'hard' transitions are the primary cause of performance loss. The full 4x4 feed network adds another 16 'hard' transitions. The S-parameter data further demonstrates the effect of these 'hard' transitions. Each output port in this case is losing almost half of its ideal delivered power due to reflections.

This data shows the inefficiency of the original feed network design. As array size is increased, losses will increase as well. Because of this, improvements to the feed network are necessary. As the simulation results show, the leading contributing factor to an inefficient feed network is impedance mismatch. The two most popular ways of dealing with mismatch between two transmission lines is quarter-wave transformers and tapering techniques. The theory of these two techniques has already been discussed in Chapter 3. Demonstration of their practical application is shown below.

A section of the feed network that includes a 'hard' transition was simulated and then compared to a section of the same length which incorporates a quarter-wave transformer. The figure below depicts the layout of both the 'hard' transition and the quarter-wave transition. Notice that the total length of the transition is just long enough to incorporate the quarter-wave section, which prevents one from having to increase the overall antenna array size.
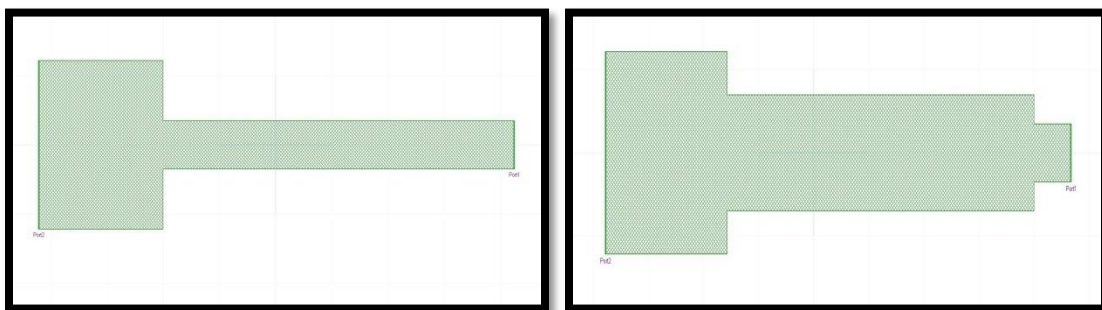

Figure 35: (a) 'Hard' Transition (b) Quarter-wave Transition

Both of these transitions were simulated in Designer and the results are shown in the figure below. The quarter-wave transformation shows an improvement over the entire band and a significant improvement of almost 6 dB at 10 GHz. The reason for the odd shape of the quarter-wave curve is the short ends of transmission line on each end of the quarter-wave section. Ideally, one would want the sections to be longer but because the objective here is to insert the quarter-wave transformer without changing overall length, this cannot be changed.
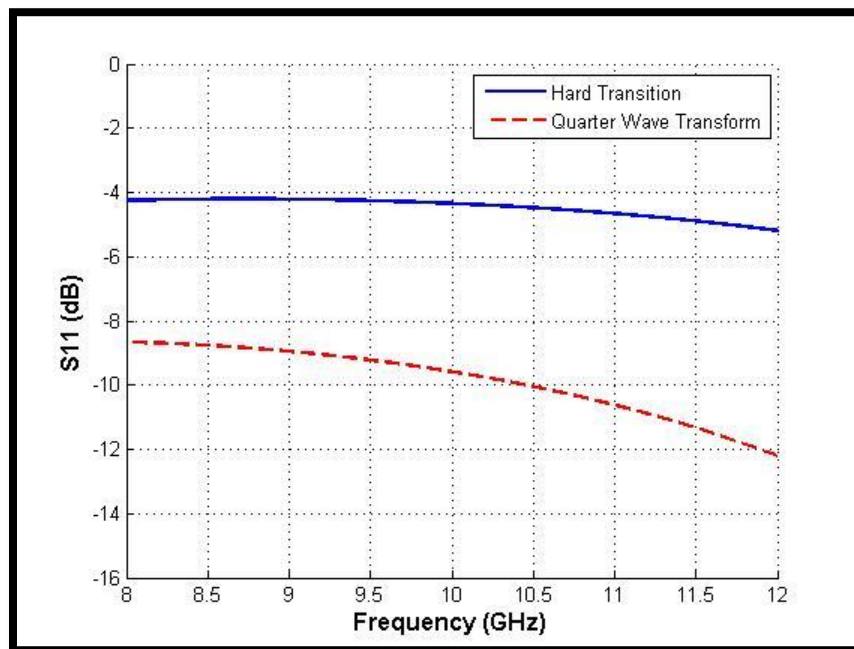

Figure 36: 'Hard' vs. Quarter-wave Transition

The other matching technique to be investigated is transmission line tapering. This technique can be used in place of or in conjunction with quarter-wave transformer techniques.   The tapered line matching technique comes from a special case of multi-section matching transformers. When designing a multisection transformer, as the number of sections, N increase, so does the step change in characteristic impedance between the sections.   As N approaches infinity the transition begins to look like a

continuously tapered line. Several specific tapering techniques exist such as the exponential taper, triangular taper, and Klopfenstein taper [4]. The only drawback in using these specific tapers in an antenna feed network design is that they are very length dependant and often times the required length for a good design exceeds the available real estate in the feed network. Regardless, a tapering technique was investigated to determine if it would provide an improvement over 'hard' transitions even in cases of short lengths. The figure below illustrates the 'hard' transition and new, tapered transition.
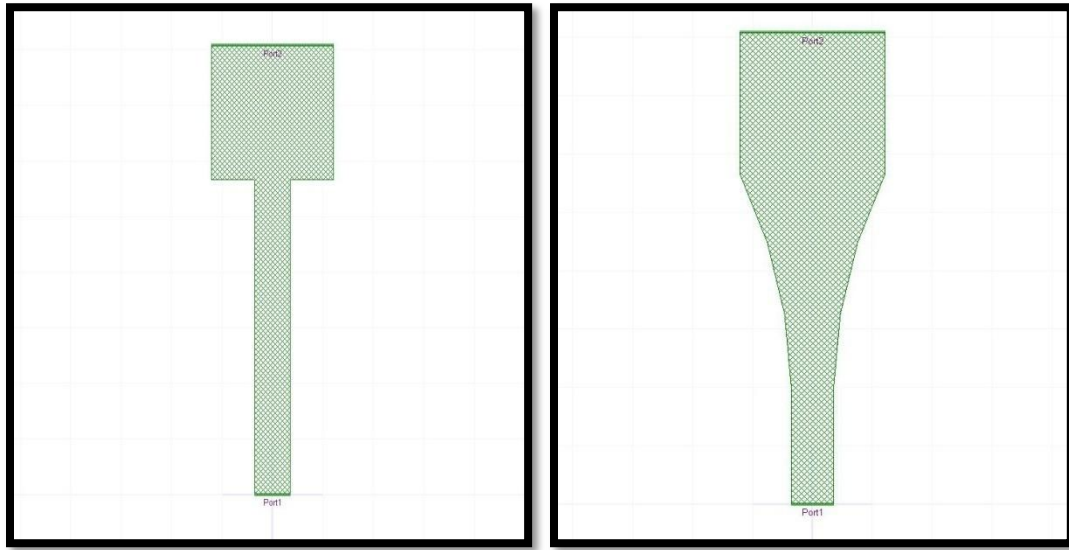

Figure 37: (a) 'Hard' Transition (b) Tapered Transition

Since the length of the transition does not allow for a traditional taper such as Klopfenstein, Designer was used to parameterize the taper with bend radius as the variable of interest to determine what taper minimizes reflection. Figure 38 shows S_{11} as a function of frequency for several bend radii.
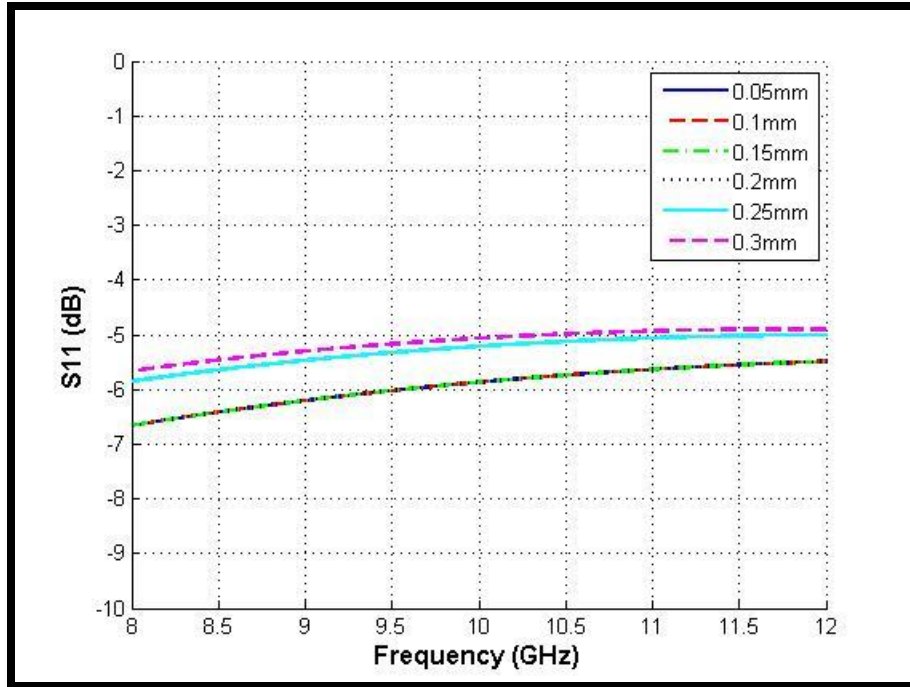
Figure 38: Parametric Analysis of Tapered Transition

The data shows that the shape of the taper does not greatly affect the transmission characteristics. Smaller bend radius values do have a slight improvement over larger values. A bend radius value of 0.25 mm was used for comparison to the 'hard' transition as shown the figure below. The improvement in using a tapered transition over such a small length compared to a 'hard' transition is small. If a bend radius of 0.2 or below had been used then the difference between the two transitions would be around 2 dB. Although not a significant difference when comparing one transition, if applied to a large feed network the tapered transitions will help reduce the overall loss due to mismatch.
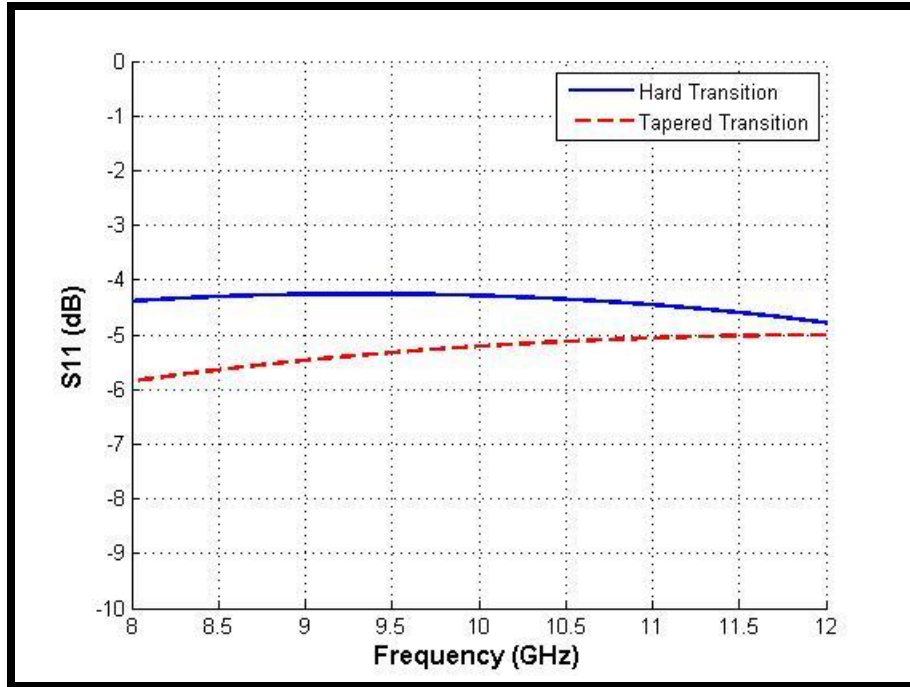
66

Figure 39: 'Hard' vs. Tapered Transition

Taking the results of the quarter-wave and tapered transition simulations into account, the original feed network was modified to incorporate these transitions in place of any found 'hard' transitions. This was manually done using the drawing capabilities available with the Designer software. The original feed network being used for this comparison has an element spacing of 18.6 mm. This spacing allows for insertion of quarter-wave transformers in place of 'hard' transitions before the final eight T-dividers. The remaining 'hard' transition connecting the feed ports were replaced with tapered transitions. The following figure is the final 16 port (4x4) feed network after all design changes were made.
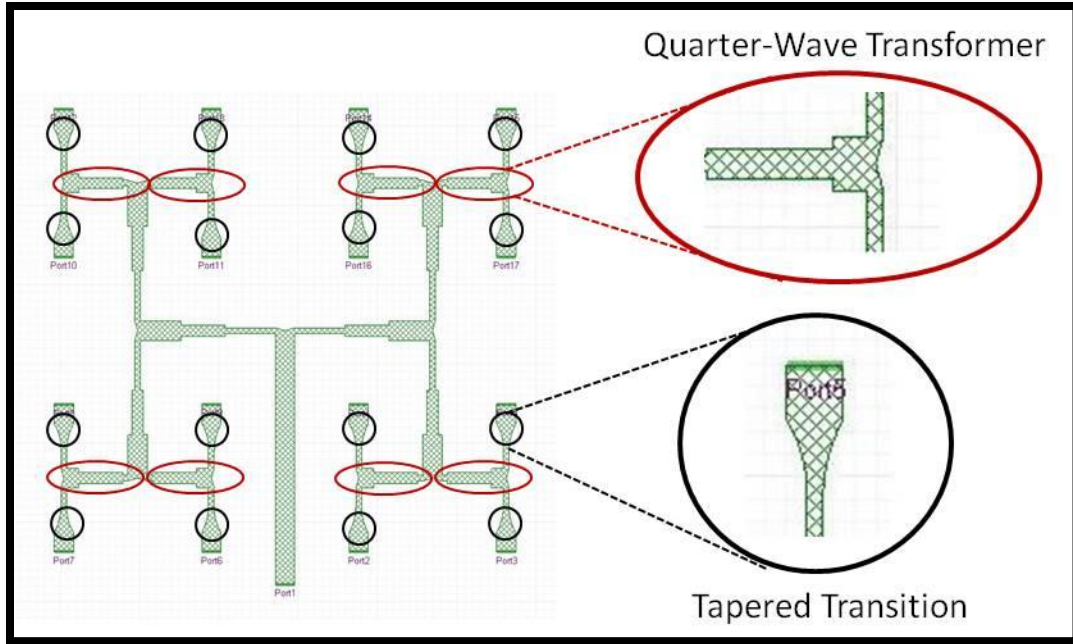
Figure 40: Revised 4x4 Feed Network

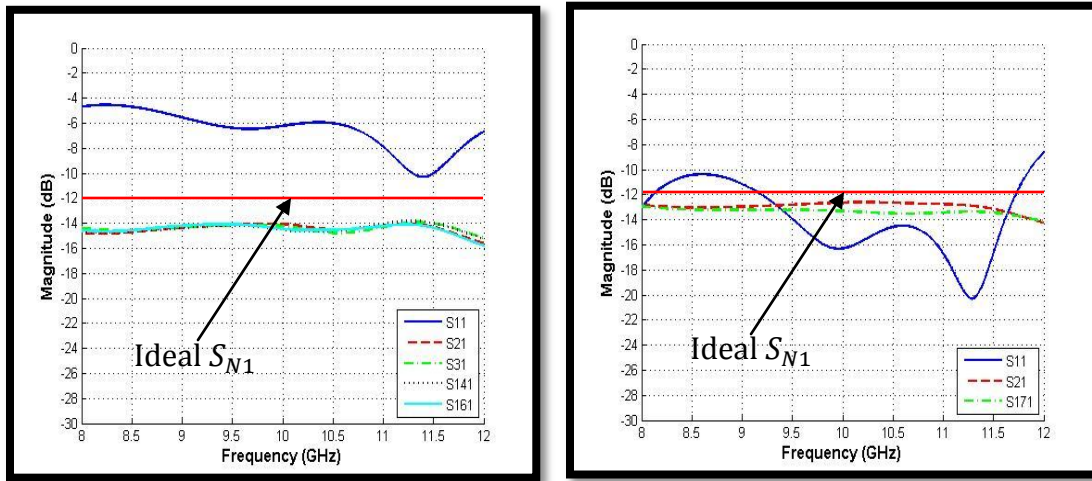**Figure 41: Original vs. Revised 4x4 S-Parmeter Data**

If compared to the original 4x4 feed network S-parameter results, it is seen that a large improvement is gained. At 10 GHz, an improvement of over 10 dB is achieved. Based on previous results, it is expected that the bulk of the improved performance comes from the added quarter-wave transformers; however the tapered lines are also contributing

68

factors. If these design changes were carried out to a 16x16 element feed network, the improvements over a design using the original layout would be even more significant.

MICROSTRIP TO COAXIAL PIN TRANSITION

The feed structure of each DRA element is electromagnetically complex due to the transitions from microstrip to coaxial probe to DRA. Ideally, the input impedance should be matched at each transition to minimize reflected power. The impedance of the DRA element and coaxial probe are a function of their physical dimensions and thus cannot be readily changed without affecting the element radiation pattern. The microstrip line feeding each coaxial probe has a set width designed for 50Ω impedance. However, the pad geometry at the feed point has an effect on the impedance seen at the microstrip to coaxial probe transition and can be altered to achieve a better match. HFSS was used to explore various pad geometries in order to choose the layout that offers maximum performance and function.

For this study, a 50 Ω microstrip line of arbitrary length is being used to feed a single DRA element via the coaxial probe. The aluminum plate is modeled with a thickness of 1/8" and the substrate used is Rogers 5880 with $\epsilon_r = 2.2$, dielectric thickness of 0.031", and copper thickness of 35 μm. Figure 42 shows the pad geometry used in the original feed network and the reflected power from 8 to 12 GHz.
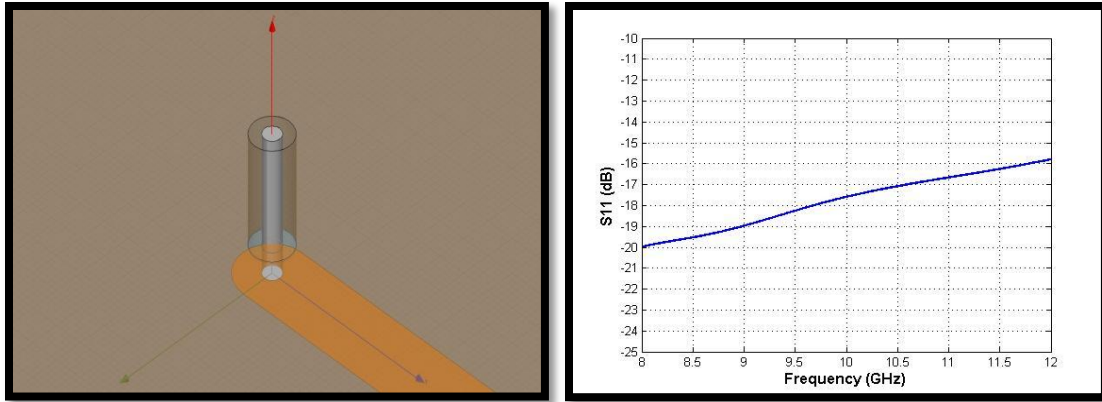
Figure 42: (a) Original Pad Layout (b) Input Port Reflected Power

In this case, the microstrip line is terminated with a semi-circular pad with diameter equal to that of the microstrip line width. The probe feed is centrally located to the diameter. The two ports for the simulation are located at the feed point of the microstrip line and at the top of the coaxial probe where it would normally feed the DRA element. All plots generated show S_{11}, which is the reflected power at the input of the microstrip feed.

The most logical choice in altering the pad geometry is to vary the pad diameter to see its effect on S_{11}. As an initial test, the pad radius was changed to 1.5mm, which results in a circular pad that is larger than the width of the microstrip line as seen in below. The simulation results directly follow and show that an increase in pad diameter results in more reflected power at the input port and thus a worse match.
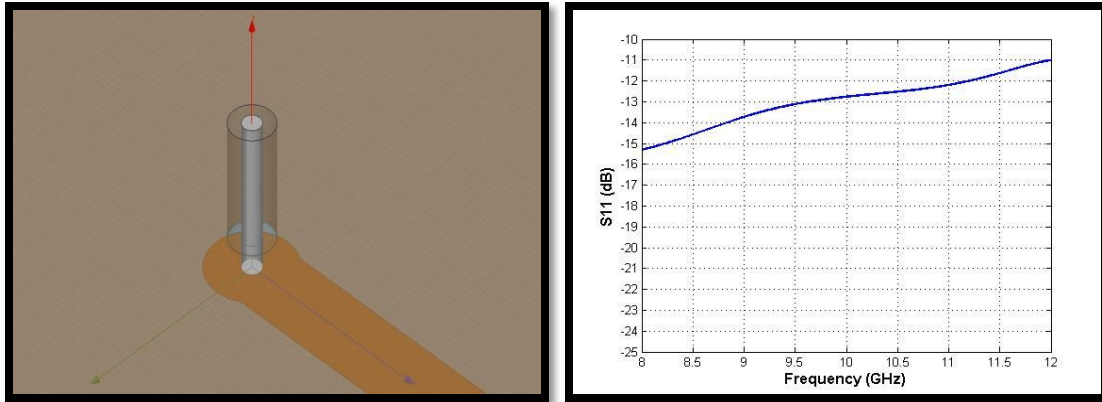
Figure 43: (a) Pad Radius = 1.5mm (b) Input Port Reflected Power

Clearly, a small change in pad radius can have a significant effect on the reflected power. A parametric analysis was run with pad radius set as the variable of interest. An arbitrary frequency near the center of the band was chosen for comparison. A clear trend was observed in that as pad radius is increased the reflected power also increases. From this, a pad radius of 0.5 mm was chosen, modeled, and simulated. The value of 0.5 mm was chosen as the smallest value which could be reasonably fabricated on the circuit mill. Figure 44 illustrates the model of this pad geometry. The coaxial probe is essentially terminated at the very end of the microstrip line with the pad serving as nothing more than a circular piece of copper to solder to. The figure also shows the results for the reflected power with the pad radius set at 0.5mm. The results demonstrate an improvement of roughly 3 dB across the entire band over the original pad geometry.
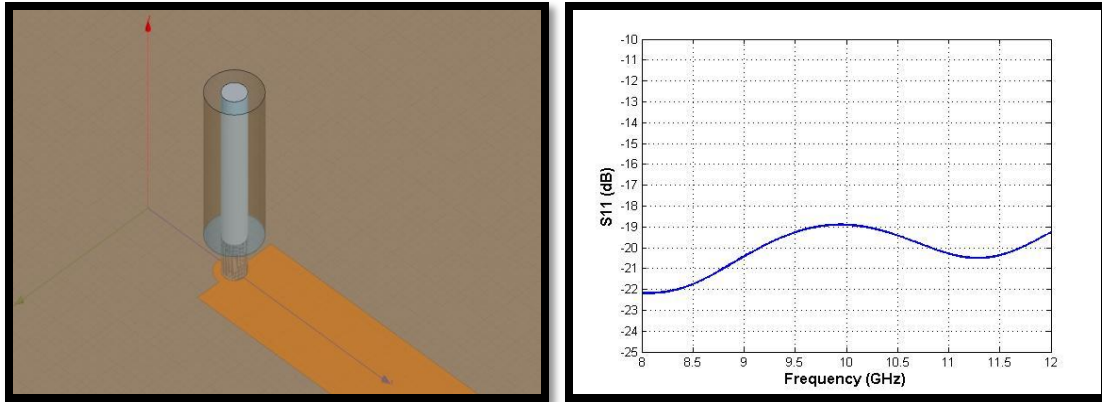
Figure 44: (a) Pad Radius = 0.5mm (b) Input Port Reflected Power

As the simulation results have shown, a small pad radius is obviously desirable over a large pad. To extend this even further, the circular pad was completely removed from the model. In this scenario, the coaxial pin is terminated at the very end of the microstrip line. The results for this design are given in Figure 45.   As expected the results are an improvement over the case where even the smallest pad radius of 0.5 mm is used. Although an improvement in performance is seen in this case, it would be difficult to manufacture with accurate precision and structural integrity. The small pad allows for solder to flow uniformly around the coaxial pin providing a solid connection. This would prove more difficult with the no pad design.
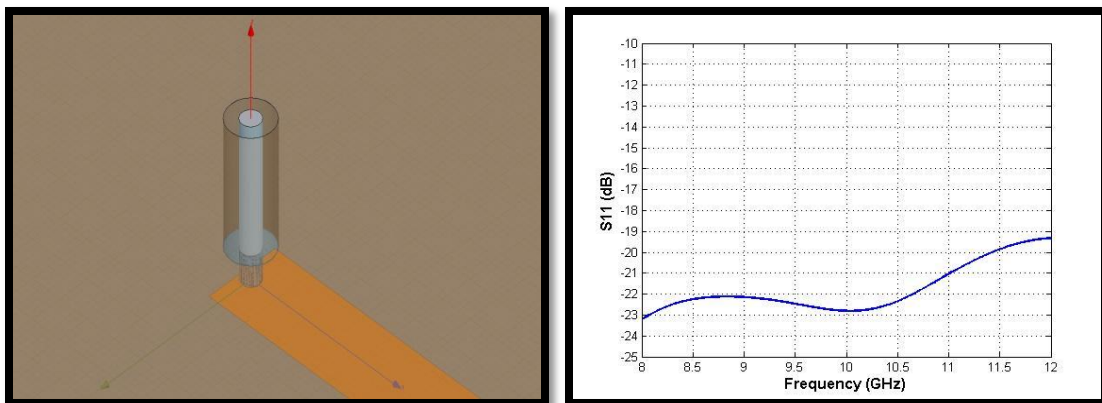

Figure 45: (a) No Pad (b) Input Port Reflected Power

72

The last design investigated is that of a tapered microstrip transition. The purpose of this is to see if there is an improvement when the microstrip line is gradually tapered from 50Ω width to a 0.5mm pad. The taper was actually parameterized and the figure below shows the geometry that provided the optimum results.
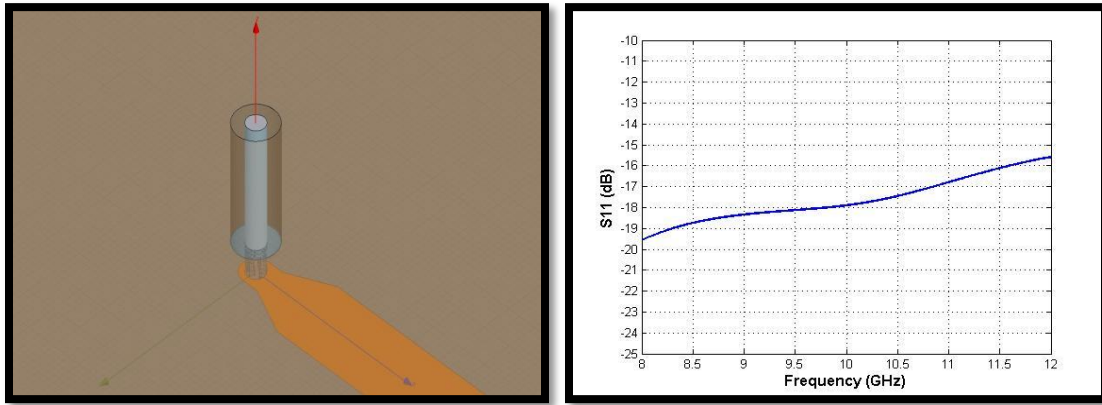

Figure 46: (a) Tapered Transition (b) Input Port Reflected Power

The results of Figure 46 show an improvement over the original design, but no improvement over the non-tapered small pad geometry. After comparing each design for performance and manufacturing feasibility, the 0.5 mm small pad geometry was chosen for the final feed network design.

With the feed network transitions and the microstrip to coaxial transition optimized, the feed network is ready to be milled and attached to the DRA array with confidence that it will deliver maximum energy to each radiating element. As mentioned previously one of the DRA's most promising feature is its high efficiency. An antenna array's total efficiency is not only dependent on the antenna element efficiency but also the efficiency of the power delivery mechanism a.k.a feed network, so this is why it is so important to design a good wide-band feed network.

FABRICATION AND TESTING OF THE DRA ARRAY

The fabrication of the DRA array has been a large reason for its slow entrance into practical commercial and military applications. The process is typically either cost prohibitive or too difficult to maintain the tolerances required to produce an effective antenna. The ceramic material typically used for DRAs because of its inherent benefits is very difficult to machine and assemble in the large geometric patterns required for an array. Using a novel fabrication technique developed during this research, three 4x4 DRA arrays and two 16x16 arrays were produced. A short discussion on the fabrication process will be detailed below.

The DRA array itself begins with a 5 mm thick sheet of Arlon's AD1000 woven glass reinforced laminate bonded to a 1/8" thick sheet of aluminum. The aluminum cladding serves as both structural support for the array and the ground plane. A CNC mill is used in the machining process to cut out the cylindrical DRA elements and to drill the coaxial air gap holes and probe feed holes. A fixture was developed to secure the array during the machining process. The DRA array is then mounted to the fixture with the substrate material facing up for milling. The cylindrical elements are formed by milling away all excess material leaving only the DRA 'pucks'. The resulting elements will have near identical dimensional properties, still be rigidly bound to the aluminum backplane, and the

array spacing is maintained to incredible accuracy. The DRA array is then flipped in order to drill the coaxial air gaps and probe feed holes. Both the depth and diameter of these holes are kept within very small tolerances due to the computer controlled precision of the CNC mill. The four pictures below show the flow of this manufacturing process.
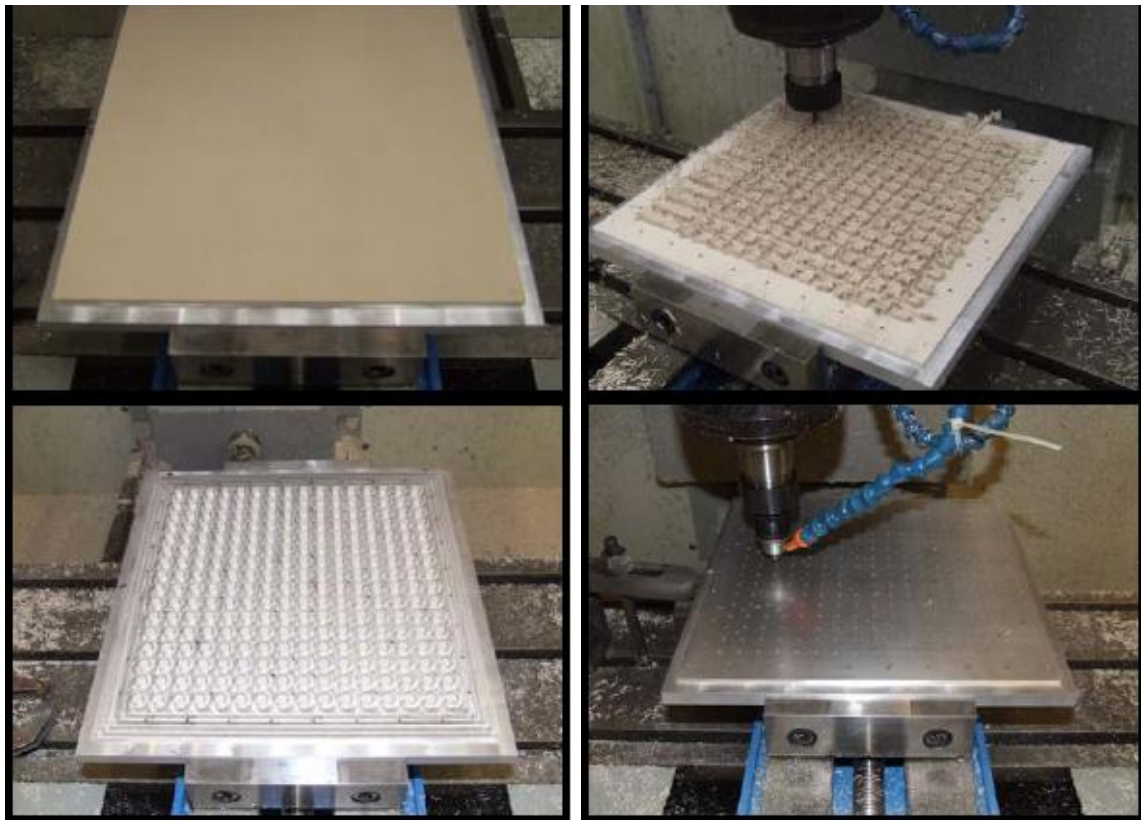
Figure 47: DRA Array Fabrication Process

The other aspect of DRA array fabrication is manufacturing of the feed network. The feed network is cut using a Quick-Circuit mill. First, a fine drill bit is used to mill around the feed structure maintaining good tolerance. Next, a larger drill bit is used to mill away all the remaining copper. The material is then flipped in order to mill the circular clearance for the coaxial line and the probe holes. The feed network is finally cut out using a contour router bit. The pictures below show the feed network being milled and the finished 16x16 feed network.
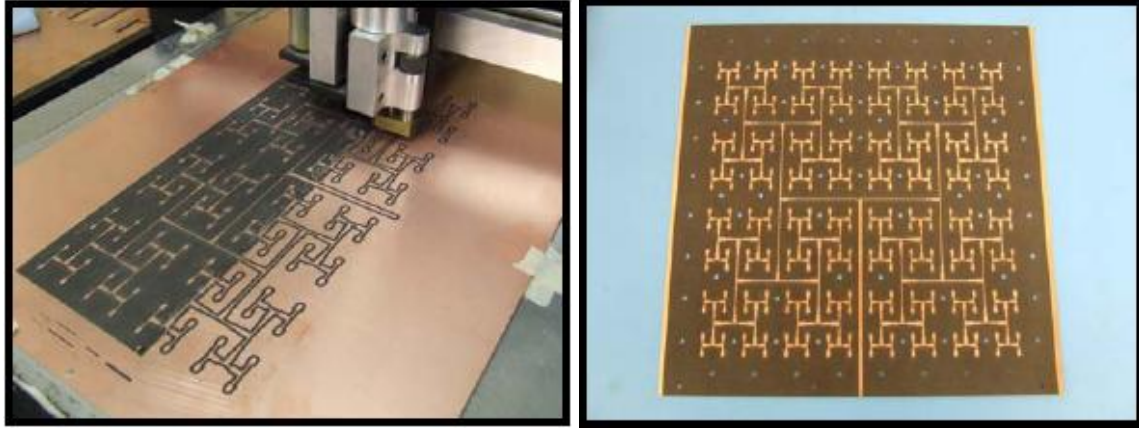
Figure 48: Feed Network Fabrication

The final stage of assembly is to attach the feed network to the face of the aluminum DRA backplane.   Several mounting holes are included to ensure a secure flush mate between the two planar structures reducing any possible air gaps. The silver probes are then fed through each feed point of the feed network until they are firmly in place inside the DRA elements.   This is a tedious process as it is done manually for each element. Finally, each probe is soldered into place on the corresponding microstrip pad on the feed network. The pictures below show the front and rear sections of a completed 16x16 DRA array assembly.

Figure 49: (a) 16x16 DRA Rear (b) 16x16 DRA Front

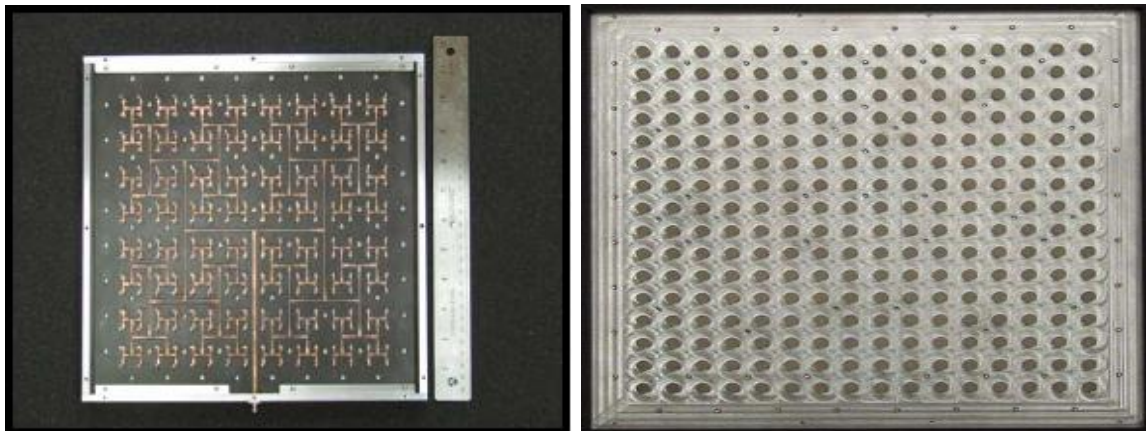One may notice the aluminum frame shown in Figure 49. These frames were designed to not only provide protection and a rigid structure but also to reduce sidelobe and rearlobe radiation. It has been shown that side walls extending above the ground plane spaced approximately $\frac{1}{2}\lambda$ away from the outer elements can reduce unwanted rearlobes and sidelobes [37-38].

Once the arrays were completed, they were tested with an Agilent Vector Network Analyzer (VNA). This was done to validate functionality of the antennas and to also give a crude validation of the simulated performance by way of return loss measurements. The reason for this being a crude validation is that the measurement is not being done inside an anechoic chamber, so reflected radiation energy can't be ignored and the HFSS simulations did not include the effects of the feed network. The figure below shows the test setup for the VNA antenna measurements.
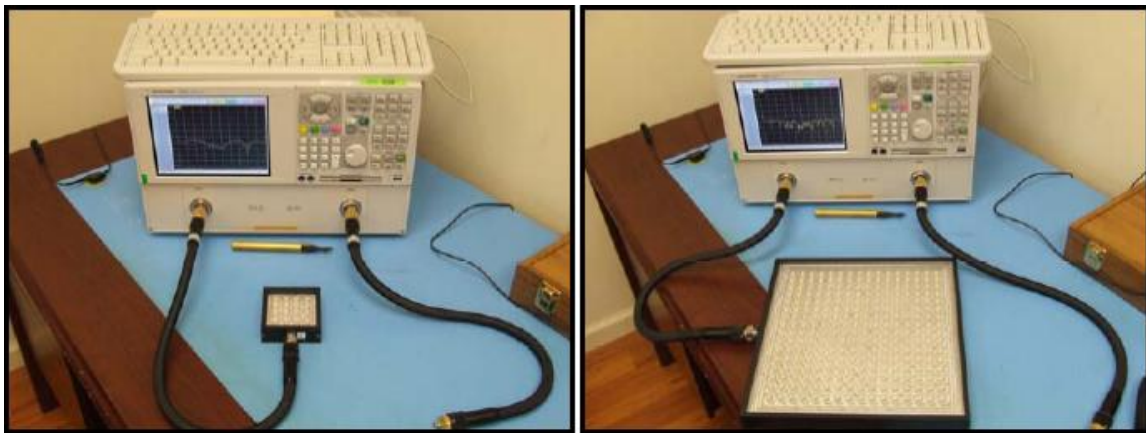

Figure 50: VNA Validation Tests for (a) 4x4 and (b) 16x16 DRA Arrays

Before manufacturing the 4x4 and 16x16 arrays, a single DRA element with a microstrip feed was fabricated. This single DRA element was tested on the VNA and compared to the HFSS simulations results for a single DRA of the same dimensions. The return loss was plotted in Matlab for comparison.
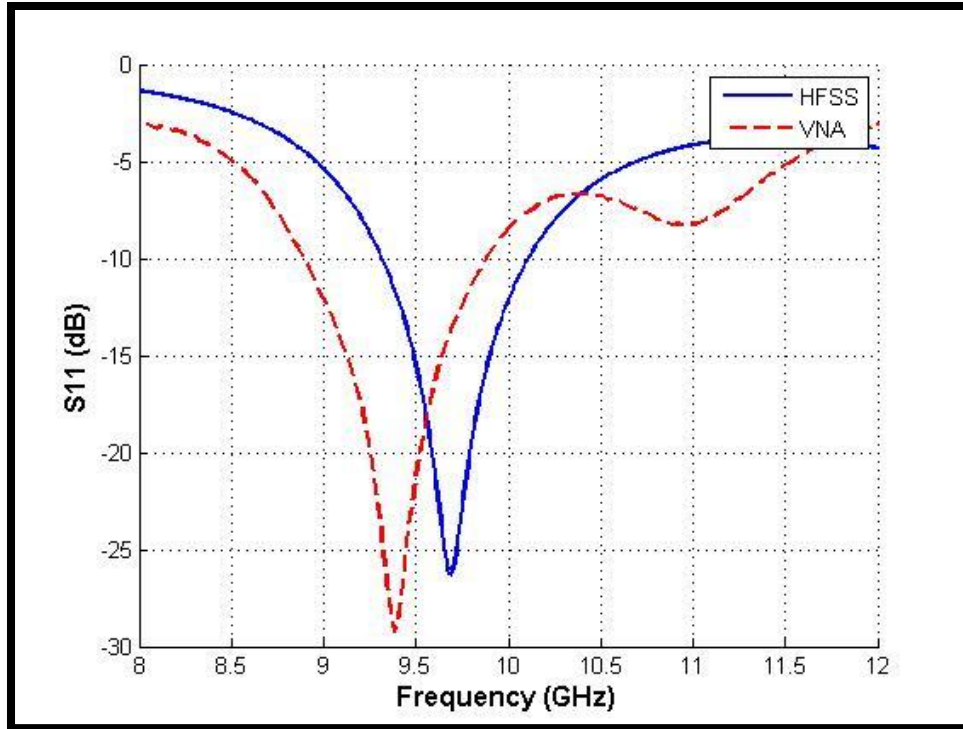
Figure 51: Single DRA Return Loss - Simulation vs. Measurement

There is a shift in resonant frequency between simulation and measurement of the single DRA most likely due to the absence of the microstrip feed and aluminum frame in the HFSS simulations. Although shifted in frequency, the bandwidth and return loss agree between measurement and simulation. At the very least, this measurement shows that HFSS can be used to design a practical x-band DRA.

The same measurement procedure was done for the 4x4 and 16x16 arrays. Unfortunately, these results can not be compared to simulation results, because there is no S_{11} data available for the entire array, only individual elements within the array, which are effected by mutual coupling. The measurement results are shown below. A sharp resonance with wide bandwidth is seen at around 10 GHz for the 4x4 array. There is also another sharp resonance at ~11 GHz. The multiple resonances in the 16x16 array are due

78

to the multiple transitions in the larger feed network. The largest resonance is still around 10 GHz, which is promising.
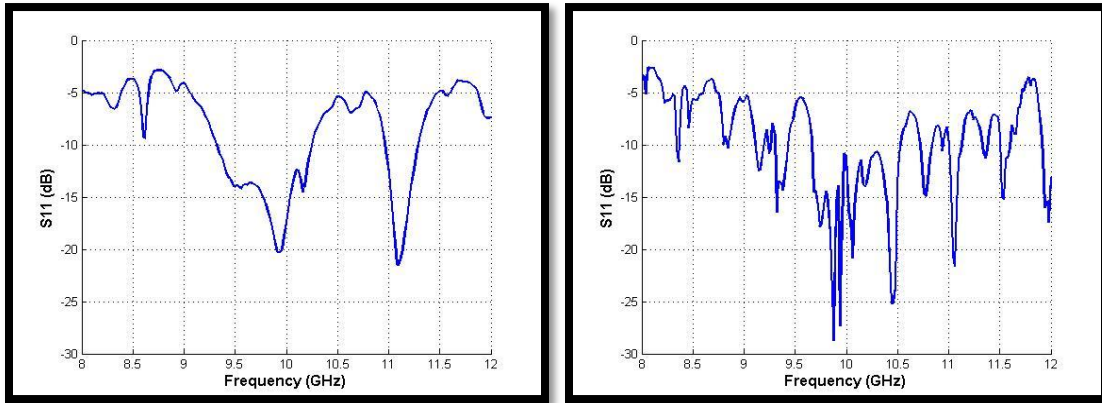

Figure 52: (a) 4x4 and (b) 16x16 VNA Measurements

A total of 5 DRA arrays were manufactured; 3 4x4 arrays and 2 16x16 arrays. All of these have the same element dimensions and spacings. The only difference between them are manufacturing tolerances in both the DRA array and the feed network. These antennas were tested using a StarLabs spherical near-field range at Satimo testing laboratories in Atlanta, GA. This system operates up to 18 GHz and has numerous capabilities. It is a spherical near-field system which uses 16 dual-polarized probes to switch electronically in elevation. The device under test (DUT) is rotated in azimuth, generating the 3-d volumetric near-field pattern, which is then processed to derive the far-field antenna pattern over the entire sphere. It reports standard antenna data such as gain, directivity, 3D radiation pattern, beamwidth, cross polar discrimination, sidelobe levels, and efficiency. Perhaps its greatest benefit over traditional near-field ranges is its ability to test an antenna in a few minutes as compared to hours for some systems. The only drawback of this system is that the maximum DUT size is limited to 45cm, but the 16x16 antenna array is only 30cm in its largest dimension so this is not a problem.

Each antenna was given a serial number to discriminate between the two 16x16 and three 4x4 arrays. The 16x16 arrays were labeled with Serial #1 and #2, and the 4x4 arrays Serial #3, #4, and #5. Antenna measurements were made in 10 MHz steps from 8.0 to 12.0 GHz. The measurement data is presented in the plots below to allow visual comparison between each of the 4x4 arrays and the 16x16 arrays, respectively. For each set of antennas the efficiency and peak gain versus frequency is provided. The far-field gain versus azimuth and elevation are also provided at the center frequency of 10 GHz to illustrate beamwidth and pattern shape.
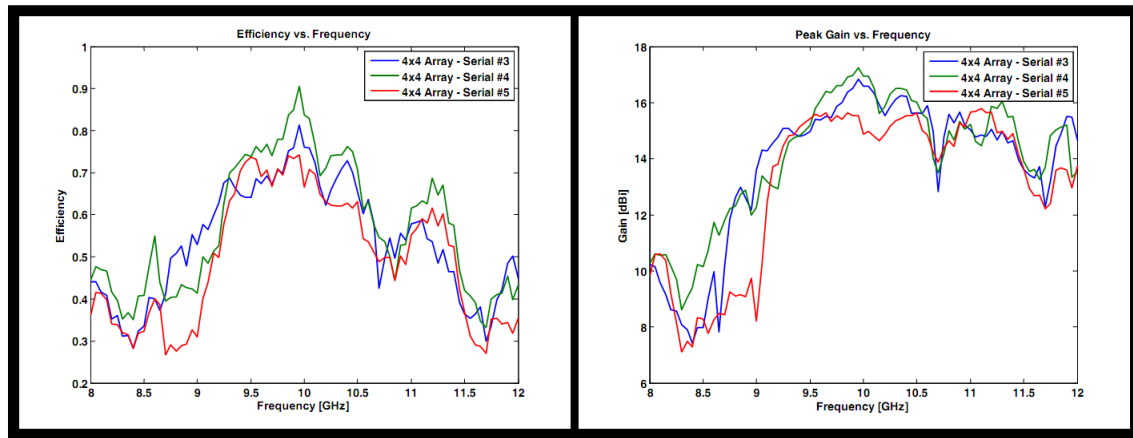

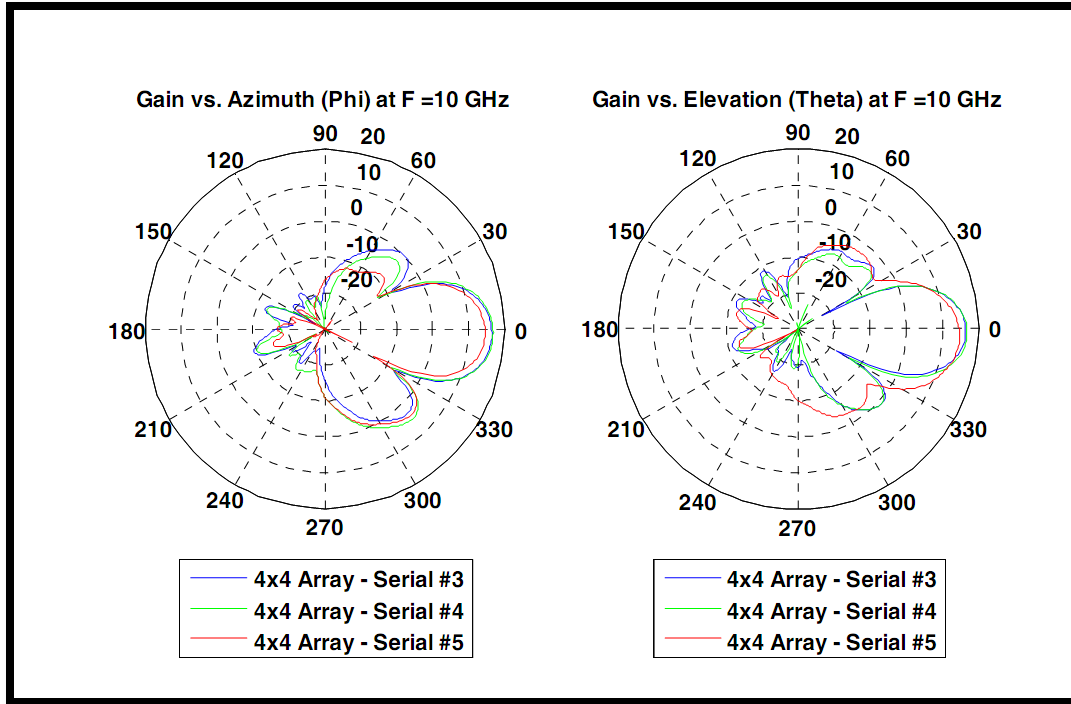**Figure 53: 4x4 DRA Array (a) Efficiency and (b) Peak Gain vs. Frequency**

Figure 54: 4x4 DRA Array Far-Field Gain vs. (a) Azimuth (b) Elevation
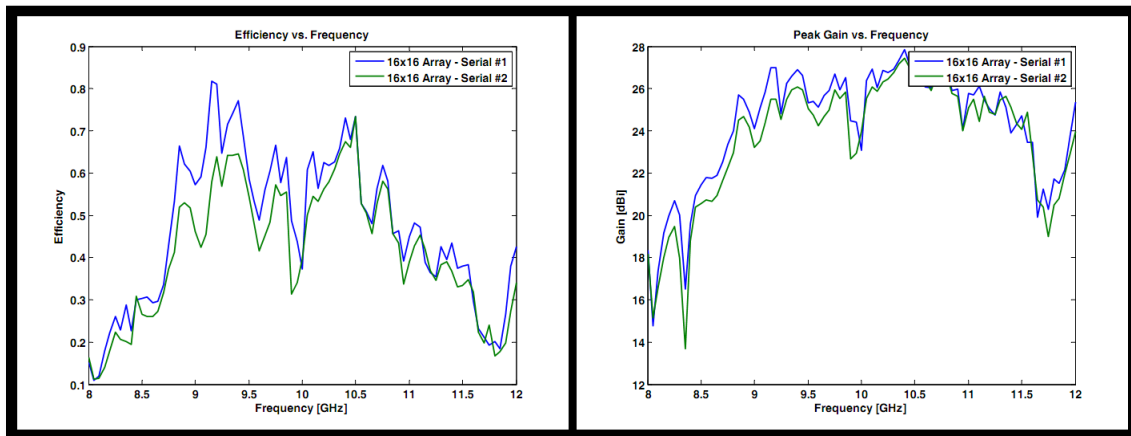
Figure 55: 16x16 DRA Array (a) Efficiency and (b) Peak Gain vs. Frequency
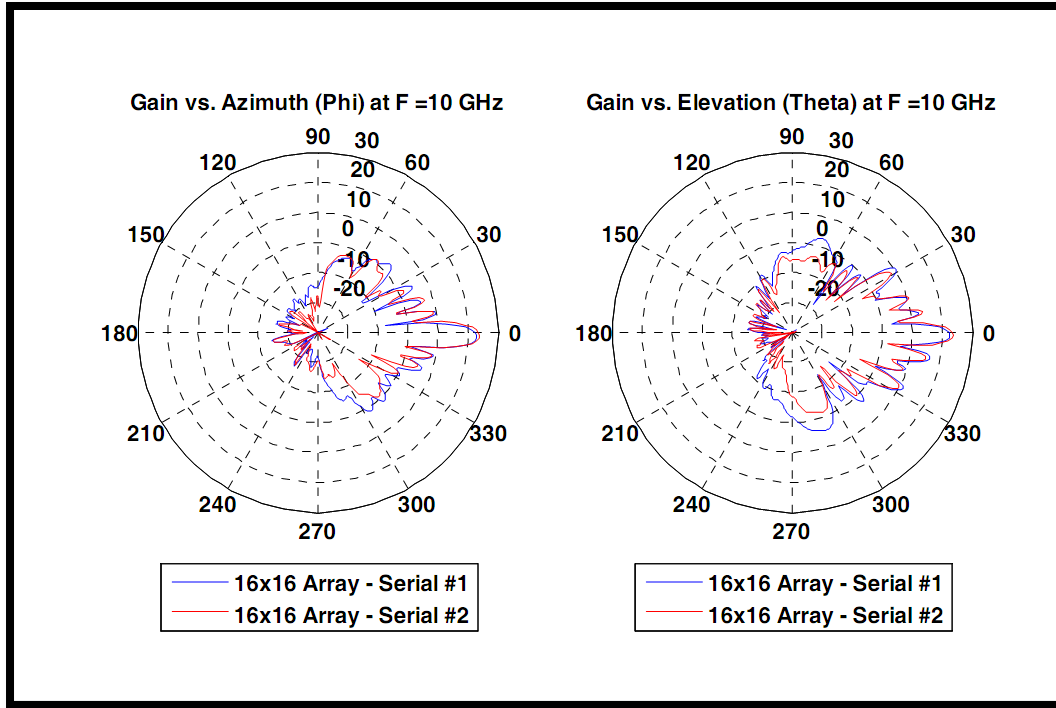
Figure 56: 16x16 DRA Array Far-Field Gain vs. (a) Azimuth (b) Elevation

The performance of the 4x4 arrays will be discussed first. The near-field data of Figure 53 shows a peak efficiency of approximately 90% and a peak gain of greater than 17 dBi at 10 GHz. For a planar antenna with a surface area less than 64 cm^2 this is quite good. The corresponding radiation pattern of the 4x4 arrays at 10 GHz shows a 3 dB beamwidth of 24° which agrees with theoretical and simulated predictions. Also, the maximum sidelobe level is 14 dB below boresight gain. For the case of the small 4x4 array, the results support the design predictions and illustrate how well an optimized DRA array can perform. There are subtle differences between the measurements of the three 4x4 arrays. This reaffirms the fact that repeatable manufacturing of DRA arrays is still a problem. Although there is high confidence in the tolerances of the DRA elements and the feed network, the probe hole location and depth is extremely difficult to keep consistent, especially across a large array.

Following the analysis of the 4x4 array, an inspection of the larger 16x16 array reveals an unexpected phenomenon. It is apparent from the efficiency and peak gain versus frequency data in Figure 55 that the operational band and performance of the large arrays are following a similar trend to that of the small arrays. Expectedly a higher gain is exhibited, peaking above 27.5 dBi, along with a correspondingly narrower bandwidth of 6°. The unexpected anomaly is the strong dip in the efficiency and gain curves around the 10 GHz design frequency. As alluded to in Chapter 4, optimal design of large arrays is currently impeded by the amount of processing power available to fully simulate the entire array. The effects of mutual coupling are prevalent in the large array configurations and this effect cannot be accurately simulated with a scaled-down model. Another potential reason for the discrepancy is the feed network. In both Designer simulations and VNA measurements, an effect on resonant frequency can be seen as the number of transitions in the feed network is increased. Because the 16x16 feed network can not be readily simulated along with the DRA elements in a full wave solver, a direct comparison can't be made between measurements and simulation. Another possible source of error could have been in the calibration of the NF range. Since these measurements were done by Satimo test engineers, the validity of the results is dependent on them correctly setting up and calibrating the test chamber. It could be possible that the receiver was saturated at 10 GHz, thus producing the unexpected drop in amplitude.

For a better analysis of the performance of the 16x16 array, the far-field radiation pattern was plotted at 10.5 GHz, which showed the best efficiency and peak gain. A 6° beamwidth is achieved along with moderate sidelobe suppression of 17 dB in azimuth and a peak gain of more than 27.5 dBi.
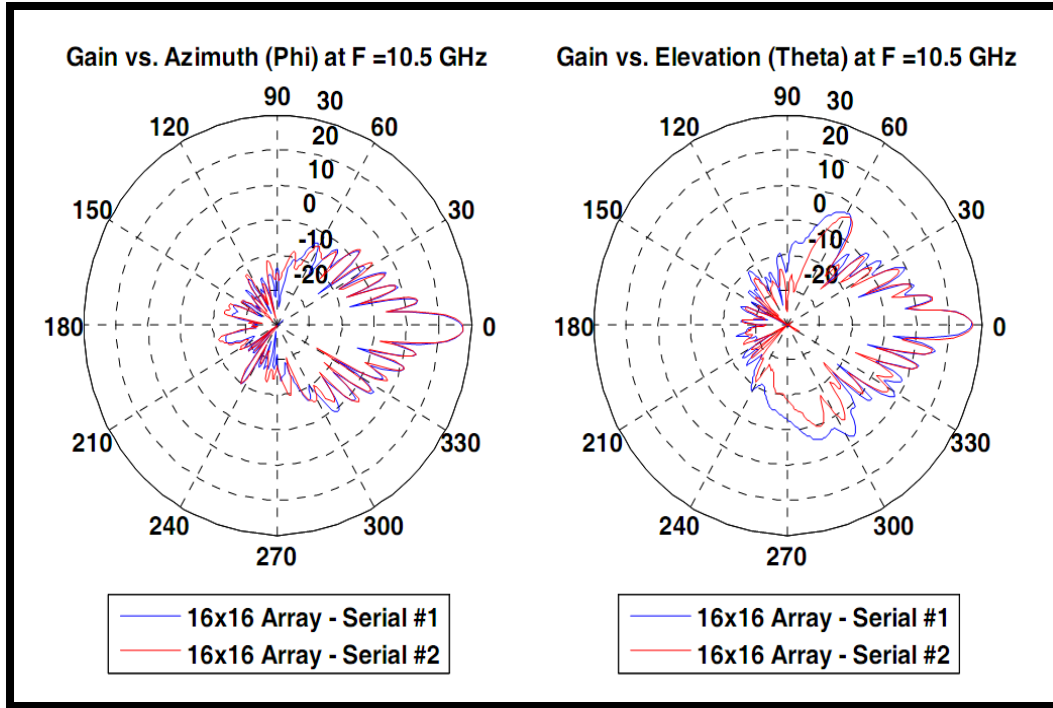
Figure 57: 16x16 DRA Array Far-Field Gain vs. (a) Azimuth (b) Elevation (10.5 GHz)

At 10.5 GHz, the 16x16 DRA array can be compared to a commercial off the shelf (COTS) patch antenna array from MTI Wireless Edge (Model# MT-30021/B). The COTS antenna exhibits a peak gain of 25 dBi and 8° beamwidth at 10.5 GHz with a bandwidth of roughly 500 MHz. The 16x16 DRA array of this research outperforms the COTS antenna while occupying a surface area approximately 10% less than that of the COTS antenna. This goes to show that DRA technology is not only competitive with current commercial patch antennas, but exceeds them in performance, especially if using a fully optimized design.

Table 4: COTS Patch Array vs. 16x16 DRA Array

Performance Parameter	MT-30021/B Patch Antenna	16x16 DRA Array
Peak Gain	25 dBi	27.85 dBi
-3dB Beamwidth	8°	7°
Bandwidth	500 MHz	600 MHz

As previously discussed, there were unexpected results around 10 GHz for the 16x16 arrays. The 16x16 arrays were measured again using a different near-field range. The near-field range used for the second measurement was a planar near-field range located at the University of Mississippi. An x-band standard gain horn (SGH) was first measured as a reference to calculate the gain of the DRA arrays. The peak gain vs. frequency is plotted for both arrays in Figure 58. Plots of the gain vs. ϕ at $\theta = 0$ for 10 GHz and 10.5 GHz follow.
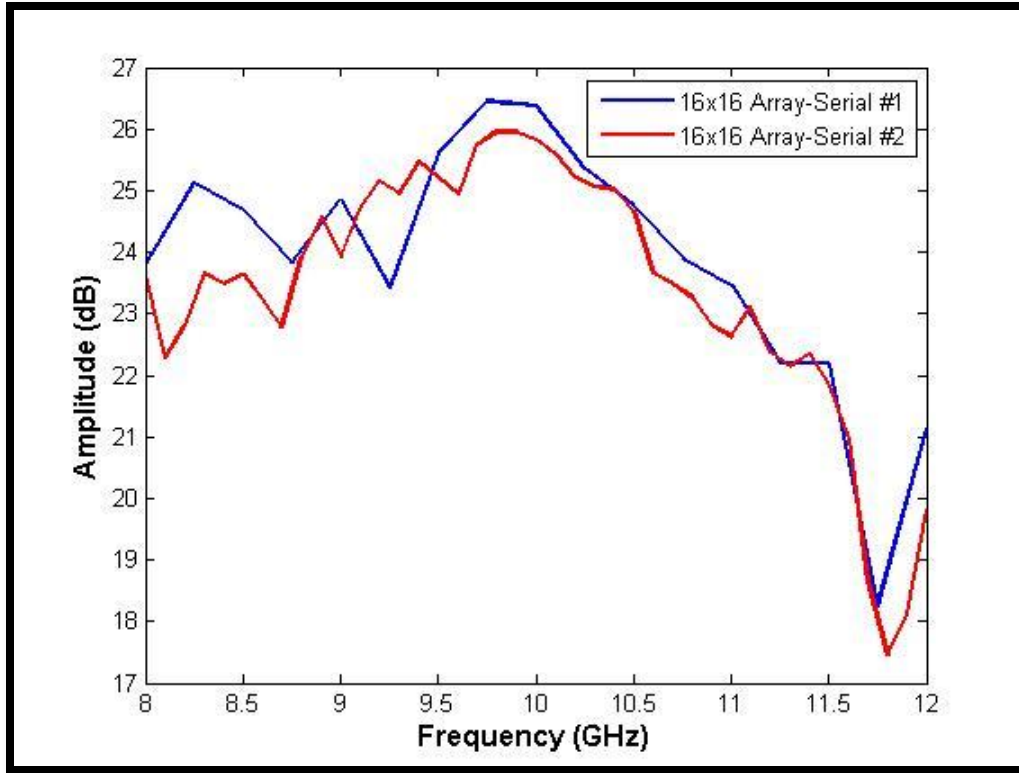
Figure 58: Planar Near-Field-Peak Gain vs. Frequency
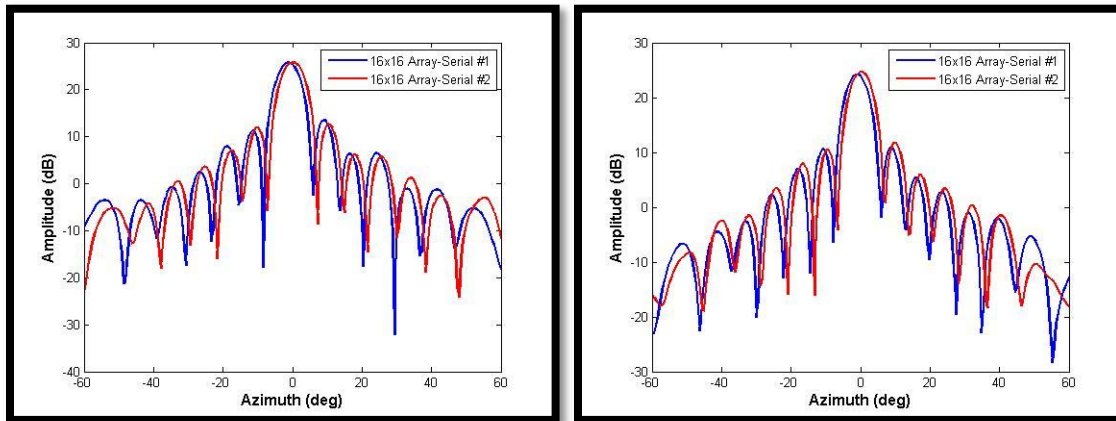
Figure 59: Planar Near-Field-Gain vs. Azimuth (a) 10.0 GHz (b) 10.5 GHz

As seen from these figures, the peak gain occurs around 9.75 to 10.0 GHz which is the design frequency. Other than the 10 GHz point, the peak gain vs. frequency plot from the planar near-field range very closely matches the peak gain vs. frequency plot from the Satimo spherical near-field range. This leads one to believe that there was indeed a

problem with the Satimo measurements and that the 16x16 DRA arrays perform quite well at their design frequency.

CONCLUSION

Although the use of the DRA array in practical fielded systems is limited, this work shows that with a well thought out design flow, commercial simulation tools, and a novel manufacturing method, the DRA array can be competitive with current generation commercial antennas using other technology.

This thesis demonstrated all aspects of a successful DRA design. Fundamental concepts such as antenna theory and transmission line theory were presented in order to provide a foundation for DRA and feed network design. Past and current literature was reviewed to establish both a history and current state of DRA technology. After establishing this foundation with theory and research, the design process began with the design and optimization of a single DRA element. Upon achieving acceptable results, a 16 element array was modeled in HFSS. This model served as a building block for the larger 256 element array. The 16 element array was used to investigate the effects of element spacing on mutual coupling and how the radiation pattern changed with operating frequency. The 256 element array was then simulated using master and slave boundary conditions, again optimizing for element spacing and radiation pattern.

An extensive analysis was performed on the feed network. As discussed, the feed network is a vital component to the antenna array and any discontinuities must be

minimized. Using Ansoft Designer software, optimizations were run on the various transitions in the feed network. Results showed that by replacing certain 'hard' transitions with quarter-wave and tapered transitions, an improvement of 10 dB could be achieved at 10 GHz. The microstrip pad to coaxial transition was also optimized to improve the transmission characteristics at this junction.

Fabrication of the DRA arrays and feed networks were discussed, including the novel DRA array fabrication techniques which produces extremely tight tolerances. Three 4x4 arrays and two 16x16 arrays were fabricated and tested in a spherical near-field range where plots of efficiency, peak gain, and radiation pattern were produced. The results of the 4x4 arrays showed good efficiency, gain, and bandwidth, which agreed with simulation results. The 16x16 arrays also showed good results, but at a higher 10.5 GHz frequency. Remeasuring the 16x16 arrays using a planar near-field range proved that the designs did indeed perform well at the design frequency of 9.75-10.0 GHz. The 16x16 arrays were compared to a commercial patch antenna array and exceeded its performance with a smaller footprint.

The work of this thesis is only a starting point for successfully implementing DRA arrays for practical use. Clearly, from the results of the 16x16 array more focus needs to be paid to mutual coupling of large arrays. A more robust numerical solution tailored for a specific array design may be needed to fully simulate the larger arrays, as the capabilities of current commercial software requires unreasonable computing resources. Further improvements to the feed network could also be made with follow on work. The Wilkinson power divider was briefly looked at in replacing the standard T-dividers in the feed network. It was decided that the increased difficulty in fabrication was not worth the

bandwidth enhancements of the Wilkinson power divider. At the current state of DRA technology, the DRAs themselves are the limiting bandwidth factor, but as research in DRA bandwidth improvement techniques continues, there may be a need to employ bandwidth enhancement techniques to the feed network. Sidelobe level is another metric that could be significantly improved and implementing power tapering techniques to the feed network could be another area to explore.

There have been recent attempts to develop computer-aids to facilitate the DRA design process [16]. As the evolution of DRA technology goes forward tools such as these and systematic processes such as the one presented in this research should help ease the burden of complex DRA array designs. The promise of dielectric resonators as antenna elements has been demonstrated and much work is still needed to push this technology to a widely used practical state.

LIST OF REFERENCES

LIST OF REFERENCES

[1] W. L. Stutzman, G.A. Thiele, Antenna Theory and Design. 2nd Edition, New York: John Wiley & Sons, Inc., 1998.

[2] C. A. Balanis, Advanced Engineering Electromagnetics. New York: John Wiley & Sons, Inc., 1989.

[3] "Antenna-theory.com", Available: http://www.antenna-theory.com/. [Accessed March 9, 2010].

[4] D. M. Pozar, Microwave Engineering. 3rd Edition, New York: John Wiley & Sons, Inc., 2005.

[5] Various Authors, "Wikipedia > Antenna (radio)" [Online encyclopedia], Available: http://en.wikipedia.org/wiki/Antenna_(radio). [Accessed March 9, 2010].

[6] H.A. Wheeler, "Fundamental Limits of Small Antennas." *Proceedings of The I.R.E. (IEEE)*, December 1947, pp. 1479-1484.

 [7] G. Breed, "Basic Principles of Electrically Small Antennas," [Online document], *High Frequency Electronics*, 2007, February, Available: http://www.highfrequencyelectronics.com/Archives/Feb07/HFE0207_tutorial.pdf. [Accessed March 9, 2010].

[8] K. Carver, J. Mink, "Microstrip Antenna Technology." *IEEE Transactions on Antennas and Propagation,* 1981, **AP-29**, pp. 2-24.

[9] D. Pozar, D. Schaubert, Microstrip Antennas - The Analysis and Design of Microstrip Antennas and Arrays. New York, NY, IEEE Press, 1995.

[10] G. J. K. Moernaut, D. Orban, "The Basics of Antenna Arrays," [Online document], 2006, Jul, 14, Available: http://www.orbanmicrowave.com/The_Basics_of_Antenna_Arrays.pdf. [Accessed October, 11, 2010].

[11] "Microwaves101.com", Available: http://www.microwaves101.com/. [Accessed November 13, 2010].

[12] D. Kajfez, P. Guillon, Dielectric Resonators. Norwood, MA: Artech House, 1986.

[13] K. M. Luk, K. W. Leung, Dielecric Resonator Antennas. Baldock, Hertfordshire, England: Research Studies Press Ltd., 2003.

[14] S. A. Long, M. W. McAllister, and L. C. Shen, "The Resonant Cylindrical Dielectric Cavity Antenna." *IEEE Transactions on Antennas and Propagation,* 1983, AP-31, 3, pp. 406-412.

[15] A. Petosa, Dielectric Resonator Antenna Handbook. Boston, MA: Artech House Inc., 2007.

[16] A. Perron, T. A. Denidni, A. R. Sebak, "Computer-Aided Design and Analysis of Dielectric Resonator Antennas." *International Journal of RF and Microwave Computer-Aided Engineering,* January 2010, vol. 20, 1, pp. 42-50.

[17] G. P. Junker, A. A. Kishk, A. W. Glisson, "Input Impedance of Dielectric Resonator Antennas Excited by a Coaxial Probe." *IEEE Transactions on Antennas and* Propagation, July 1994, vol. 42, 7, pp. 960-965.

[18] R. A. Kranenburg, S. A. Long, J. T. Williams, "Coplanar Waveguide Excitation of Dielectric Resonator Antennas." *IEEE Transactions on Antennas and Propagations*, January 1991, vol. 39, 1, pp. 119-122.

[19] J. T. Martin, Y. M. Antar, A. A. Kishk, A. Ittipiboon, M. Cuhaci, "Dielectric Resonator Antenna Using Aperture Coupling." *Electronics Letters,* November 1990, vol. 26, 24, pp. 2015-2016.

[20] I. A. Eshrah, A. A. Kishk, A. B. Yakovlev, A. W. Glisson, "Theory and Implementation of Dielectric Resonator Antenna Excited by a Waveguide Slot." *IEEE Transactions on Antennas and Propagation,* January 2005, vol. 53, 1, pp. 483-494.

[21] A. A. Kishk, "Experimental Study of Broadband Embedded Dielectric Resonator Antennas Excited by a Narrow Slot." *IEEE Antennas and Wireless Propagation Letters,* 2005, vol. 4, pp. 79-81.

[22] R. Chair, A. A. Kishk, K. F. Lee, "Wideband Simple Cylindrical Dielectric Resonator Antennas." *IEEE Microwave and Wireless Components Letters,* April 2005, vol. 15, 4, pp. 241-243.

[23] A. A. Kishk, R. Chair, K. F. Lee, "Broadband Dielectric Resonator Antennas Excited by L-Shaped Probe." *IEEE Transactions on Antennas and Propagation,* August 2006, vol. 54, 8, pp. 2182-2189.

[24] Y. Coulibaly, T. A. Denidni, "Design of a Broadband Hybrid Dielectric Resonator Antenna for X-band Applications." *Journal of Electromagnetic Waves and Applications,* 2006, vol. 20, 12, pp. 1629-1642.

[25] A. Petosa, A. Ittipiboon, Y. M. M. Antar, D. Roscoe, M. Cuhaci, "Recent Advances in Dielectric-Resonator Antenna Technology." *IEEE Antennas and Propagations Magazine,* June 1998, vol. 40, 3, pp. 35-48.

[26] A. Buerkle, K. F. Brakora, K. S. Sarabandi, "Fabrication of a DRA Array using Ceramic Stereolithography." *IEEE Antennas and Wireless Propagation Letters,* 2006, vol. 5, pp. 479-482.

[27] A. Petosa, S. Thirakoune, M. Zuliani, A. Ittipiboon, "Comparison Between Planar Arrays of Perforated DRAs and Microstrip Patches." *Antennas and Propagation Society International Symposium, 2005 IEEE,* July 2005, vol. 2A, pp. 168-175.

[28] R. Chair, A. A. Kishk, K. F. Lee, "Comparative Study on the Mutual Coupling Between Different Sized Cylindrical Dielectric Resonators Antennas and Circular Microstrip Patch Antennas." *IEEE Transactions on Antennas and Propagation,* March 2005, vol. 53, 3, pp. 1011-1019.

[29] L. K. Hady, A. A. Kishk, D. Kajfez, "Dual Band Dielectric Resonator Antenna for GPS and WLAN Applications." *Microwave Conference, 2008. APMC 2008. Asia-Pacific,* December 2008, pp. 1-4.

[30] S. G. O'Keefe, S. P. Kingsley, "Tunability of Liquid Dielectric Resonator Antennas." *IEEE Antennas and Wireless Propagation Letters,* 2007, vol. 6, pp. 533-536.

[31] T. Edwards, Foundations for Microstrip Circuit Design. 2nd Edition, Baffins Lane, Chinchester, England: John Wiley & Sons, 1992.

[32] G. Kompa, Practical Microstrip Design and Applications. Norwood, MA: Artech House, Inc., 2005.

[33] HFSS Software is distributed by the Ansoft Corp., http://www.ansoft.com.

[34] E. Levine, "A Study of Microstrip Array Antennas with the Feed Network." *IEEE Transactions on Antennas and Propagation,* April 1989, vol. 37, 4, pp. 426-434.

[35] S. Demir, C. Toker, "Optimum Design of Feed Structures for High G/T Passive and Active Antenna Arrays." *IEEE Transactions on Antennas and Propagation,* March 1999, vol. 47, 3, pp. 443-452.

[36] H. Schuman, J. Cummins, "Practical Feed Network Design for Antenna Arrays." *IEEE Transactions on Antennas and Propagation,* November 1973, vol. 21, 6, pp. 862-864.

[37] R. Marg, I. Schön, A. F. Jacob, "Finite Ground Plane Effects on the Radiation Pattern of Small Microstrip Arrays." *IEE Procedings-Microwave Antennas and Propagations,* April 2000, vol. 147, 2, pp. 139-143.

[38] K. Kona, M. Manteghi, Y. Rahmat-Samii, "A Novel Dual-Frequency Dual Polarized Stacked Patch Microstrip Array Feed for Remote Sensing Reflector Antennas." *Microwave and Optical Technology Letters,* July 2006, vol. 48, 7, pp. 1250-1258.

VITA

John Ashmore was born in Tupelo, MS in 1982. At an early age he developed a great interest in mathematics and computer technology. He graduated from W.P. Daniel High School in 2000 with a 4.0 GPA and was awarded a full paid scholarship to attend Northeast Mississippi Community College. John studied computer science the two years he attended NEMCC and earned a full paid scholarship to the University of Mississippi with his academic accomplishments.

At the University of Mississippi, John changed his major from computer science to electrical engineering with an emphasis in computer engineering. This decision was based on his evolving interest in engineering and also his desire for a challenge. While studying engineering, John worked part-time as an IT specialist for the USDA National Sedimentation Laboratory. John was involved in several clubs and organizations while at the University of Mississippi. This included serving as president of the Eta Kappa Nu honor society and vice-president of the IEEE Ole Miss student section. John was awarded the Eta Kappa Nu outstanding Junior award in 2004 and the Mississippi Engineering Society Outstanding Engineering Senior award in 2005. In the spring of 2005, he obtained his B.S. degree in electrical engineering, summa cum laude.

Upon graduation John accepted a position as an electrical engineer with Radiance Technologies in Oxford, MS. During the four and a half years employed with Radiance

Technologies John worked on projects ranging from antenna design and simulation to x-band radar development. In August of 2005 John enrolled in the University of Mississippi electrical engineering graduate program under the guidance of Dr. Elliott Hutchcraft and Dr. Richard Gordon. His primary areas of interest during this time were electromagnetic modeling using the finite element method and radial basis functions, and also dielectric resonator antenna design. John completed his coursework for his masters degree while working full time at Radiance Technologies.

In February of 2010, John accepted a job with Dynetics in Huntsville, AL. John currently supports his government customers working as a radar engineer. He hopes to have a long successful career as an electrical engineer and continue to expand upon his technical knowledge with a lifetime of research and learning.